Master of Science Thesis

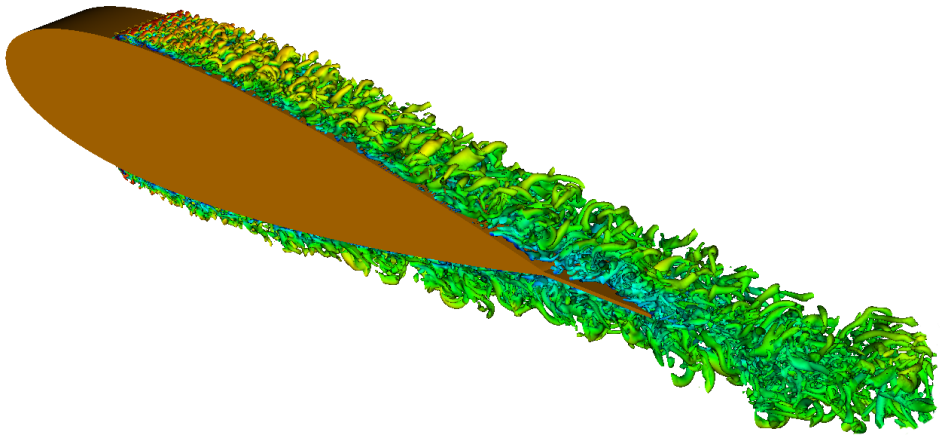

Computational aeroacoustic analysis of trailing edge noise

A Direct Numerical Simulation using the Lattice Boltzmann Method

Jaap Rooks

August 10, 2016

Aerodynamics

TU Delft

Faculty of Aerospace Engineering

Delft University of Technology

Computational aeroacoustic analysis of trailing edge noise

A Direct Numerical Simulation using the Lattice Boltzmann Method

Master of Science Thesis

For obtaining the degree of Master of Science in Aerospace Engineering
at Delft University of Technology

Jaap Rooks

August 10, 2016

Faculty of Aerospace Engineering · Delft University of Technology

Delft University of Technology

DELFT UNIVERSITY OF TECHNOLOGY
DEPARTMENT OF AERODYNAMICS

The undersigned hereby certify that they have read and recommend to the Faculty of Aerospace Engineering for acceptance the thesis entitled **"Computational aeroacoustic analysis of trailing edge noise"** by **Jaap Rooks** in fulfilment of the requirements for the degree of **Master of Science**.

Dated: August 10, 2016

Supervisors:

Prof. Dr. S. Hickel

Dr. Ir. A.H. van Zuijlen

Ir. W.C.P. van der Velden

Dr. D. Ragni

Abstract

Reducing trailing edge noise for large wind turbines can potentially increase the widespread use of wind energy, providing substantial benefits for our climate. Trailing edge serrations seem to be a good method for noise source reduction, however optimisation of these add-ons require a deeper understanding of the physics behind trailing edge noise. This objective of this thesis is to aid the development for improved trailing edge serrations for trailing edge noise reduction by analysing trailing edge noise source generation and propagation.

In this study direct numerical simulations are performed on a NACA 0018 wing section with and without trailing edge serrations using the lattice Boltzmann method. The results show that trailing edge serration effect the local flow and decrease noise by a maximum of 3 dB, and overall by around 2 dB. For high frequencies the noise was increased by around 0.5 dB.

On the basis of the observations in this thesis it can be concluded that:
Trailing edge serrations locally accelerate the boundary layer, reduce turbulent fluctuations in the flow and reduce pressure fluctuations on the trailing edge surface which reduces the noise significantly in all directions, but most dominantly upstream. The frequency at maximum noise reduction is defined by a non-dimensional Strouhal number based on the boundary layer displacement thickness at the straight trailing edge of 0.09. Noise reduction is achieved up to a value of 0.23.

The generalisation of frequency scaling can lead to better design comparisons and potentially ease the design of optimised trailing edge serrations to reduce wind turbine noise.

Preface

The purpose of computation is insight, not pictures

Lloyd N. Trefethen

After seven years of study my time at the TU Delft will finally come to an end. When I was in high school I already had the idea of doing something with aerodynamics later, preferably in the automotive industry. After my high school I started at Aerospace Engineering with this in mind. After completing my Bachelor Aerospace Engineering in three years without much trouble I started my Aerodynamics Master which I came for to this faculty.

During the four years of my Master I learnt a lot about myself; I have a much clearer view of my strengths and limitations. Although my Master didn't go as originally planned, I am truly satisfied with the results I got. I am proud to present this thesis as the final stage in obtaining my Master's degree in Aerodynamics at the Faculty of Aerospace Engineering of the Delft University of Technology.

For the last 11 months I mostly worked in the basement of the High Speed Laboratory (HSL), which was also mockingly known as the dungeon. I really liked my stay in the basement due to the great atmosphere and the people there. You could always pass by someone's desk for a little chat or for his/her opinion on a topic of your thesis. I would like to thank the people from the basement who helped me survive my thesis and making my time here extraordinary. Thank you to my (former) basement colleagues Peter, Thomas, Mirko, Jiggar, Annemiek, Emel, Matthijs, Fleur, Kitso, Remco, Koen, William, Govert, Olaf, Tariq, Piyush, Aman, Jordi, Sofia, Quan, Andrea, Deborah, Steve, Edgar, Li, Alberto and Woosik. Good luck to you all.

Thank you to my supervisors dr. ir. Sander van Zuijlen and ir. Wouter van der Velden for their support during my thesis. The regular meetings were really helpful to get better insights on the subject and the progress of the thesis. Even when we didn't had a meeting planned I could just step by your offices with my questions.

Thanks to my good friends outside of Delft for the welcome distractions during the weekends. These helped me to stop thinking about my thesis for some moments and just have fun.

I would like to thank my family. Thanks to my parents for their unconditional love and support during my study. And a special thanks to my dad for carpooling in the mornings during the beginning of my thesis.

Now that my time as a student is finally over, I hope that the future brings me more amazing and wonderful moments.

Thank you all very much!

V I E

Jaap Rooks
Delft,
August 10, 2016

Table of Contents

List of Figures

List of Tables

Nomenclature

Abbreviations

BGK	Bhatnagar-Gross-Krook
CAA	Computational Aeroacoustics
CFD	Computational Fluid Dynamics
CFL	Courant-Friedrichs-Lewy
DNC	Direct Noise Computation
DNS	Direct Numerical Simulation
FW-H	Ffowcs Williams and Hawkings
LBM	Lattice Boltzmann method
LES	Large Eddy Simulation
LGA	Lattice Gas Automata
MRT	Multiple Relaxation Time
NS	Navier-Stokes
OASPL	Overall averaged sound pressure level
PIV	Particle image velocimetry
RANS	Reynolds-Averaged Navier-Stokes
SPL	Sound pressure level
VR	Volume of refinement

Greek

Δt	Time step increment

Δx	(Local) lattice spacing
δ	Boundary layer thickness
δ^*	Boundary layer displacement thickness
δ_{100}	Boundary layer thickness for 100% of free stream edge velocity
δ_{99}	Boundary layer thickness for 99% of free stream edge velocity
δ_{ij}	Kronecker delta
$\delta()$	Dirac delta function
η	Kolmogorov scale
λ	Wavelength
λ_2	Second invariant of the velocity tensor
ν	Kinematic viscosity
Ω_i	Rate of change of the particle distribution function due to collision
ω_i	Weights corresponding to the lattice velocity vectors
Φ_{aa}	Aeroacoustic sound pressure level
$\hat{\rho}$	Non-dimensional density
ρ	Macroscopic density
ρ'	Density relative to the density at rest
ρ_0	Density at rest
ρ_s	Reference density
τ	Relaxation time parameter
τ_{ij}	Viscous stress tensor

Roman

a_0	Speed of sound
b	Spanwise length
C_s	Physical speed of sound
c_s	Speed of sound of the lattice system
$\boldsymbol{c}_i$	Discrete velocity vector in the ith direction
$\boldsymbol{e}_i$	Lattice velocity vectors
f	Frequency

f_i	Particle distribution function in direction i
f_i^{eq}	Distribution function at local equilibrium
H	Kinematic shape factor
h_{trip}	Height of transition strip
L	Characteristic body length
l	Characteristic length scale
l_0	Scale of largest eddies
L_s	Characteristic length scale
l_{trip}	Length of transition strip
M	Mach number
N	Number of mesh cells
n_i	Outward unit normal from the fluid
p	Macroscopic pressure
p_0	Pressure at rest
$\hat{r}$	Non-dimensional length
r	Radial distance between the source and the observer
$\mathcal{R}e$	Reynolds number
s_{trip}	Span of one zig-zag transition strip
St	Strouhal number
$\hat{t}$	Non-dimensional time
T_{ij}	Lighthill stress tensor
$\bar{u}$	Time-averaged x-velocity
$\hat{u}$	Non-dimensional velocity
U	Flow velocity
u_e	Boundary layer edge velocity
U_s	Characteristic velocity
$\boldsymbol{u}$	Macroscopic velocity
$\boldsymbol{x}$	Distance between origin and observer
y^+	Dimensionless wall distance
$\boldsymbol{y}$	Distance between origin and sound source

Chapter 1

Introduction

Climate change is increasingly recognised as one of the most critical challenges ever to face humankind. In order to reduce greenhouse gas emissions that contribute to this climate change, the demand for renewable energy is increasing due to international agreements in the last few decades. One way to harvest renewable energy is by using wind turbines. Although wind turbines might seem a good solution to generate renewable energy, controversy exists about placement of wind turbines near inhabited places, due to for example noise nuisance. Governments apply noise regulations for maximum allowable noise levels for wind turbines near inhabited places, which are generally stricter at night. These noise regulations limit the power output of wind turbines, which leads to a reduction in the annual energy production. These regulations could therefore potentially stop the widespread use of wind energy. In the last few decades several researches have been conducted to quantify the wind turbine noise, e.g. Hubbard and Shepherd (1991); Guidati et al. (2000). The origin of wind turbine noise can be split into two main classes, namely mechanical noise and aeroacoustic noise. Mechanical noise is generated by different components in the hub, such as noise from the gearbox or the generator. The aeroacoustic noise is caused by the interaction between the incoming flow and the tower and/or the rotor blades. The propagation of mechanical noise can be reduced by using better isolation or sound absorbing materials in the hub and nacelle. The propagation of aeroacoustic noise sources, however, is not as straightforward to block, because the sound sources are located at the outside of the blades making isolation or absorbing materials useless. In order to reduce the aeroacoustic noise the sources should therefore be mitigated, which involves complex mechanisms. For large wind turbines, aeroacoustic noise is the most dominant noise source, and therefore better understanding of the mechanisms is key to reduce sound emissions (Oerlemans et al. (2007)).

There are several different aeroacoutic sources that can be involved in the noise production of wind turbines, of which most are due to the interaction between the incoming flow with the turbine blades, known as airfoil self-noise. This airfoil self-noise is caused by the interaction between the airfoil surface and its boundary layer and/or near wake. According to Brooks et al. (1989) five different airfoil self-noise mechanisms exist which are illustrated in Fig. 1.1.

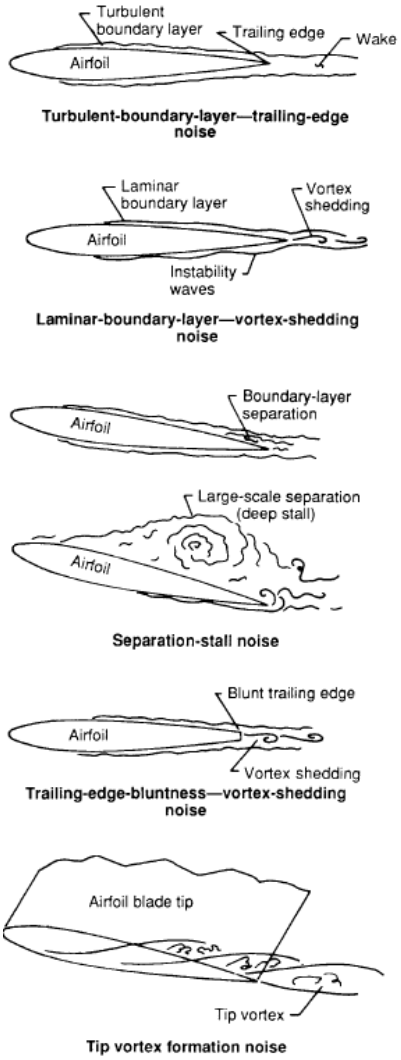

Figure 1.1: Five self-noise mechanisms identified by Brooks et al. (1989).

For each of these mechanisms a specific boundary layer phenomenon is identified (Brooks et al. (1989)). The five self-noise mechanisms are each explained in the following paragraphs.

Turbulent boundary layer trailing edge noise For large wind turbines the outer part of the blades experiences a high incoming velocity (Re $>$ 1 million). Due to this high Reynolds number the boundary layer is turbulent along the blade surface. At these design conditions the boundary layer stays attached until the trailing edge of the airfoil where it interacts with it. At the trailing edge of the wing an impedance discontinuity exists, where near field pressure fluctuations of the turbulent flow are scattered from the trailing edge, causing a broadband noise (Howe (1991a); Oerlemans (2011)). This turbulent boundary layer trailing edge noise, known as trailing edge noise, is depicted in Fig. 1.1. Trailing edge noise is considered to be the most dominant self-noise mechanism on a wind turbine(Oerlemans (2011)).

Laminar boundary layer vortex shedding noise For Reynolds number below about 1 million, a largely laminar boundary layer can exists on one surface (usually the pressure surface) of the airfoil up to the trailing edge. For certain conditions a single tone or several tones with high amplitude are produced. There are several studies done in the past which give different explanations of the mechanism behind this self-noise source.

Paterson et al. (1973) attributed the tonal noise produced by the airfoils to vortex shedding of the laminar boundary layer at the trailing edge. Other authors, such as Tam (1974), proposed that it was not vortex shedding which caused the noise but boundary layer instabilities. Tam proposed that the source of the tonal noise was due to a self-excited feedback loop between the point of first instability on the surface and a point downstream in the wake. The feedback loop found by Tam (1974) is explained further below.

The laminar boundary layer instabilities, known as Tollmien-Schlichting waves, become amplified as they move along the airfoil surface. When these waves reach the sharp trailing edge of the airfoil these instabilities propagate into the wake where they cause the wake to vibrate laterally. These vibrations emit acoustic waves that propagate in all directions. When part of the waves reach the pressure side of the airfoil near the trailing edge upstream, they reinforce the original boundary layer disturbance, completing the feedback loop (Tam (1974)).

Due to the different view of several authors compared to Brooks et al. (1989) the tonal noise generation mechanism is also called laminar boundary layer instability noise, yet referring to the same phenomenon.

In order to reduce laminar boundary layer vortex shedding noise (or instability noise) a trip may be applied to induce transition from laminar to turbulent flow. Because this self-noise mechanism is characterised by low Reynolds number flows this noise source is considered only relevant for small wind turbines.

Separation stall noise At increasing angles of attack the boundary layer on the suction side of the airfoil may separate resulting in airfoil stall. In Fig. 1.1 the different stages of stall are depicted. At moderate angles of attack the flow will separate from the trailing edge of the airfoil, producing trailing edge noise due to shed turbulent vorticity (Brooks et al. (1989)). At very high angles of attack, the separated flow near the trailing edge gives way to large-scale separation which causes the entire airfoil to emit low-frequency noise. Although this separation stall noise can be significant, it is considered of minor importance for wind turbines when pitch-control is present (Oerlemans (2011)). Large modern wind turbines are always pitch-controlled making stall noise insignificant for these turbines.

Trailing edge bluntness vortex shedding noise Blunt trailing edge noise occurs when the thickness of the trailing edge of an airfoil is larger than a critical value. Vortex shedding occurs in the form of periodic Von Kármán vortices in the small separated flow region downstream of the blunt trailing edge, which may result in a tonal noise (Oerlemans (2011)). Proper blade design and production can already prevent a blunt trailing edge, for example

by using a sufficiently small thickness for the trailing edge.

Tip vortex formation noise Tip vortex noise is different compared to the previous four airfoil self-noises as this is the only self-noise mechanism which is not related to the trailing edge. At the tip of the blade the pressure difference on the upper and lower surface cause tip vortices. Similar as for trailing edge noise, turbulent flow convects over the tip edge where it interacts with the tip surface, causing tip noise. The noise source depends on the strength of the tip vortex and the planform of the blade tip (Oerlemans (2011)).

For aircraft/helicopters the same pressure difference over the wing occurs resulting in a tip vortex. To mitigate the vortex strength and the resulting turbulence, winglets can be used to reduce the tip vortex build-up. A similar device can be applied to wind turbine blades to reduce the blade tip noise.

Inflow turbulence noise Apart from airfoil self-noise there is another mechanism that generates noise for wind turbines. Turbulence present in the oncoming flow may interact with the turbine blades and cause inflow turbulence noise. This turbulence may be generated by the wake of upwind objects or by the atmospheric boundary layer. The turbulent eddies in the flow will interact with the boundary layer of the turbine blades and cause pressure fluctuations on the surface which radiate into the far field. This inflow turbulence noise can be a large contributor of the total noise when the inflow is highly turbulent. This noise source however depends strongly on the surrounding objects and atmospheric conditions, and is therefore not easily reduced for a certain turbine site. Proper site orientation and examination however can be a solution to limit this inflow turbulence noise.

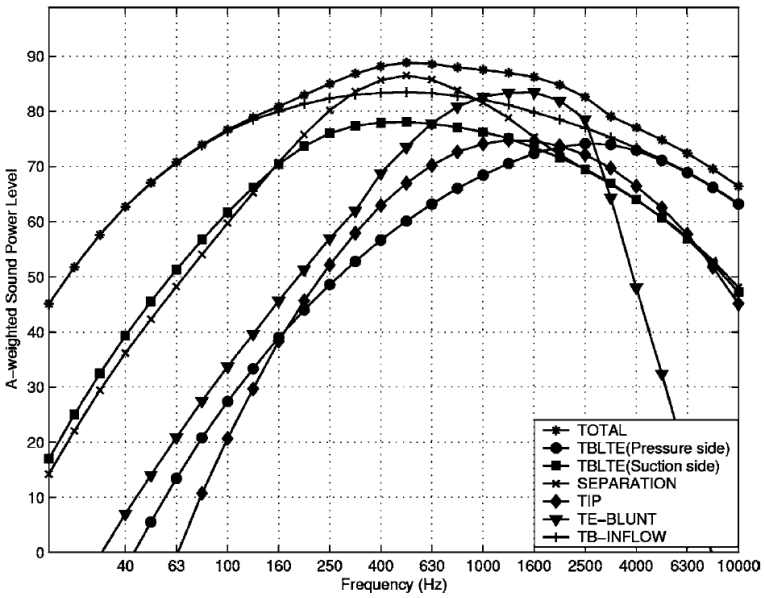

Figure 1.2: Noise spectra of different source mechanisms for a 300 kW wind turbine (From Zhu et al. (2014)).

As mentioned before, there are several different aeroacoustic sources involved in the noise production of wind turbines. Zhu et al. (2014) performed numerical computations to give an estimation of the relative strength of the source mechanisms involved. The result of the scaled sound power level, accounting for frequency dependent sensitivity of the human ear, for a 300 kW wind turbine is shown in Fig. 1.2. From this figure one can see that turbulent inflow noise is the main source of sound at low frequencies. For higher frequencies separation and trailing edge bluntness can produce more noise than the turbulent boundary layer trailing edge mechanism. However, as described above separation and blunt trailing edge noise can be easily mitigated, making trailing edge noise the most dominant source of sound in the mid to high frequency regime for large wind turbines, and therefore topic of this thesis.

1.1 Characteristics of airfoil noise

Aerodynamically generated sound propagates different in free space and in proximity of a sharp edge. A dimensional analysis performed by Lighthill (1952) shows that the free field turbulence source has a 'quadrupole' type characteristic. For a typical velocity U in the flow and a length scale l, and also for constants of the fluid such as the density ρ_0, the speed of sound a_0 and the kinematic viscosity ν_0 Lighthill produced a relation for the acoustic power of such quadrupole.

Lighthill showed that the total acoustic power, which is proportionate to the square of the acoustic pressure p, scales according to:

$$p^2 \propto \rho_0 U^8 {a_0}^{-5} l^2 \tag{1.1}$$

From this equation we can conclude that the acoustic power scales with $\rho_0 U^3 M^5 l^2$ for a turbulent eddy in the flow (away from any edge or surface).

The rate of decay of the kinetic energy of the eddy through viscous action is equal to the energy supply rate in a steadily maintained flow, and is proportional to $\rho_0 U^3 l^2$. Hence the ratio of the acoustic power output to the supply of power, which ratio can be considered the aerodynamic sound production efficiency, is of the order M^5. This means that for low Mach numbers, as for wind turbines, free turbulence is very inefficient to produce sound.

For eddies near a sharp (trailing) edge the size of the eddies with respect to the airfoil chord is important for the noise spectra. The turbulent length scale, Λ, for trailing edge noise is equal to the boundary displacement thickness, δ^* (Oerlemans (2011)). For a mean velocity of U, the disturbances occur at a frequency $f \sim U/\lambda$, which is equal to the frequency of the radiated sound $f = a_0/\lambda$, λ being the acoustic wavelength.

So if the eddies are much larger than the airfoil chord ($C/\lambda \ll 1$), the acoustic wavelength emitted will also be much larger than the chord. When this is the case the airfoil is acoustically compact. If the acoustic wavelength is much smaller than the airfoil chord, the airfoil is acoustically non-compact.

When the airfoil is acoustically compact the eddies will cause a fluctuating force on the complete airfoil, resulting in a low-frequency sound which radiates as a compact dipole (Oerlemans (2011)). The acoustic power of these eddies scales with the sixth power of the flow speed according to Curle (1955):

$$p^2 \propto \rho_0 U^6 {a_0}^{-3} l^2 \tag{1.2}$$

From this equation we can conclude that the acoustic power scales with $\rho_0 U^3 M^3 l^2$ for an acoustically compact airfoil. The efficiency of the aerodynamic sound production is therefore of order M^3, which for low Mach numbers is larger than the free turbulence noise efficiency discussed before. The radiation (or directivity) pattern is given by $p^2 \sim \sin^2\theta$, where θ is the angle with respect to the flow direction. From this it follows that the maximum radiation occurs for $\theta = 90°$, which is in the direction perpendicular to the mean flow, see Fig. 1.3.

For acoustically non-compact airfoils ($C/\lambda \gg 1$) the small eddies near the trailing edge will induce only local pressure fluctuations which do not effect the global aerodynamic field. The acoustic power generated by these small eddies follow another power law given by Ffowcs Williams and Hall (1970):

$$p^2 \propto \rho_0 U^5 {a_0}^{-2} l^2 \tag{1.3}$$

This reveals that the aerodynamic sound production efficiency for a non-compact airfoil is proportionate to M^2 which makes these high-frequency sound more efficient in noise production than the small (low-frequency) eddies. The directivity pattern for the non-compact airfoil is given by $p^2 \sim \sin^2(\theta/2)$. The maximum radiation occurs for $\theta = 180°$, which is in the upstream direction i.e. in the direction of the leading edge for trailing edge noise and in the downstream direction for leading edge noise, see Fig. 1.3.

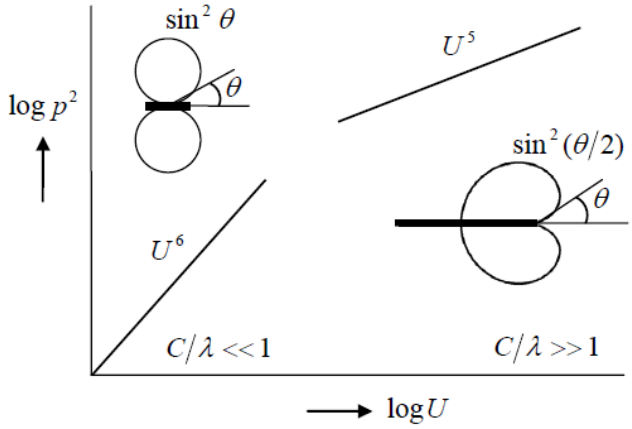

Figure 1.3: Directivity and velocity dependence of airfoil noise. (From Blake (1986)).

In Fig. 1.3 the directivity and velocity dependence of the compact and non-compact airfoil noises is presented. The compactness factor $C/\lambda \sim MC/\Lambda$, thus for given airfoil chord C and eddy length scale Λ, increasing flow velocity U changes the behavior from a compact dipole to an (non-compact) edge noise source. For trailing edge noise the turbulent length scale is of the order of δ^* which is much smaller than the airfoil chord, so $\delta^*/C \ll 1$. Hence the transition between the two acoustic regimes will occur at relatively low subsonic speeds (Blake (1986)). Because of that the trailing edge noise is expected to have a both a compact and non-compact behaviour.

1.2 Solutions to trailing edge noise

In the past decades several studies have been performed to qualify and quantify trailing edge noise, including solutions to reduce this trailing edge noise.

Almost half a century ago Ffowcs Williams and Hall (1970) were one of the first to study the aerodynamic generated sound of a flat plate trailing edge. They used the equation derived by Lighthill (1952) which describes aerodynamic noise generation and propagation as a starting point for their analysis. Originally, Lighthill (1952) used his equation to model the problem of sound generation by turbulence in an ideal acoustic medium, i.e. without any objects. Ffowcs Williams and Hall (1970) used the Lighthill equation to the problem of sound generated by a turbulent flow near a scattering half plane. The result of this analysis was that the far field sound intensity induced by sources close to the trailing edge depend upon the fifth power of a typical fluid velocity.

Using the semi-infinite flat plate approximation Oerlemans (2011) derived the following expression for the acoustic power of (non-compact) trailing edge noise generated by a segment of the wing:

$$p^2 \sim U^5 \frac{L\delta^*}{r^2} \cos^3\gamma \sin^2(\theta/2) \sin\phi, \tag{1.4}$$

where U is the typical fluid velocity at the edge, L is the span of the wing section, δ^* the boundary layer displacement thickness at the trailing edge, and r is the radial distance between the source and the observer ($r \gg L$). The definition of the angles in the equation above are shown in Fig. 1.4.

From this equation one can see that the fifth power law found by Ffowcs Williams and Hall (1970) is also present for the semi-infinite case. The strong speed dependence of the acoustic power is the main reason why the outside part of turbine blades are the most dominant in the production of sound. The directivity pattern of the produced sound ny the semi-infinite plate is in agreement with the pattern on the right side of Fig. 1.3. The radiation is symmetrical about the chord with maximum radiation in the direction of the leading edge.

From the equation it can be concluded that in the lateral direction no sound is radiated

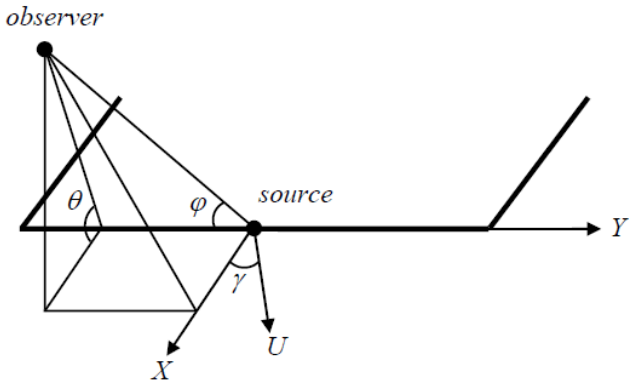

Figure 1.4: Definition of the angles in Eq. 1.4 for trailing edge noise from a semi-infinite plate. (From Oerlemans (2011)).

in the direction of the trailing edge, where $\phi = 0$. Eq. 1.4 shows that for $\gamma = 0$ the noise radiation is maximum. This angle corresponds with a flow direction perpendicular to the trailing edge of the wing. For increasing angles the factor $\cos^3\gamma$ drops, reaching a value of zero for an angle of 90°, which corresponds to the flow being parallel to the trailing edge. The interesting point from this is that applying (trailing edge) sweep to a wing might reduce the noise produced by the trailing edge.

Several decades before the research of Oerlemans (2011), Amiet (1976) and Howe (1999) calculated the far field noise produced by an airfoil with a sharp trailing edge encountering a turbulent flow. In their calculations they approximated the trailing edge as a semi-infinite flat plate, which was subject to a low Mach number flow. Amiet (1976) and Howe (1999) assumed that the initial hydrodynamic pressure fluctuations convected unchanged over the trailing edge, which acts as an impedance discontinuity, and are scattered in the form of acoustical waves. A similar directivity pattern as found by Oerlemans (2011) was obtained.

Later Howe (1991a,b) applied his theory to trailing edges with different kind of serrations ($\gamma \neq 0$) to reduce the trailing edge noise. Howe (1991a) found that for a flat plate with sinusoidal serrations of wavelength λ the high frequency noise was reduced by $10log_{10}[(2\pi h/\lambda)]$ dB compared to the straight trailing edge. Howe also showed that at low frequency the serrations do not affect the noise radiation.

According to Howe the principal noise sources are associated with elements of the edge that have an angle between the mean flow and the trailing edge of more than 45°. For a sinusoidal trailing edge this angle becomes 90° at the tops and valleys, where the flow is perpendicular to the edge. Using sawtooth serrations instead could reduce trailing edge noise further.

For the sawtooth serrations Howe (1991b) indeed found a different relation for the noise attenuation. For high frequencies the noise level reduction found for a tooth spacing of λ was $10log_{10}[1 + (4h/\lambda)^2]$ dB, which is higher than for the sinusoidal serrations. As can be seen from the equation, large slender teeth are better for sound mitigation than short wide teeth. Although his research laid the foundation of trailing edge noise reduction, his theories

overpredict the noise attenuation by such systems, especially at high frequencies ($> 2kHz$), according to other experimental studies in the last decades (e.g. Dassen et al. (1996); Petitjean et al. (2011); Oerlemans et al. (2009)).

A possible explanation for the overprediction by Howe is that the pressure difference over the wing is not taken into account in the flat plate model. The hydrodynamic behaviour in the vicinity of the serrations may change due to this pressure difference thus making the prediction inaccurate.

His theory also predicts strong oscillations in the noise spectrum which he ascribes to the interference between the root and the tip of the serrations. This however, has not been confirmed in any experimental investigation.

Based on the trailing edge noise reduction found by Howe (1991a,b) for different trailing edge serrations, multiple experimental studies are performed using these devices. Dassen et al. (1996) were one of the first to put the theory of Howe to the test by a series of wind tunnel measurements. To see if the theory of Howe was accurate for more realistic flows and geometries different types of airfoils and flat plates with varying planforms and trailing edge teeth orientations were used. The sawtooth serrations used in this study were very long and thin, $\lambda/h = 0.2$, as suggested by the theory of Howe (1991b). The noise reduction due to the sawtooth serrated flat plates were found to be up to 10 dB for a frequency of 1 kHz - 6 kHz for a freestream Mach number of $M = 0.12 - 0.22$. This large noise reduction however is still below the estimated values of up to 20 dB predicted by Howe's theory for these conditions.

The tests by Dassen et al. (1996) showed that all serrated airfoils, with and without camber, reduce the noise compared to the unserrated reference airfoils. The noise reductions found were ranging from 3 dB to 8 dB. Although this noise reduction is quite impressive, considering a 3 dB loss means a 50% reduction in acoustic power, the attenuation is significantly lower than for the flat plates. This suggests that more research should be done to understand the mechanism which drives the noise reduction for airfoils.

Later Gruber et al. (2010) extended the theory by Howe for slitted trailing edges, and performed measurements to compare the noise performance with a sawtooth trailing edge. According to their analytical solution slit serrations are not an effective noise reduction treatment due to the fact that the noise reduction asymptotes to zero at high frequencies. The experimental results showed that the noise is reduced by about 3 dB for low frequencies but is increased from about 700 Hz. Sawtooth serrations, however, reduced the noise by about 5 dB in the low and mid frequency range after which a similar increase is noticed, confirming the overprediction by Howe once more.

Recently a study by Avallone et al. (2016) is performed at TU Delft using three-dimensional measurements of the flow past three different serration designs. The measurements were done by means of time-resolved tomographic particle image velocimetry on a NACA 0018 wing at 4° angle of attack and 10 m/s free stream velocity. An array of 64 microphones has been used to gather the trailing edge noise at 30 m/s. The results show that flow is being leaked from the pressure to the suction side of the wing, destroying the turbulent coherent structures into smaller ones. This destruction of turbulence structures might be the reason for the

overprediction by Howe at high frequencies, who assumed a frozen turbulence flow convecting over the trailing edge. The destruction of the large coherent structures into smaller ones reduces the noise of low frequency noise and shifts it to the higher frequency regime, which explains why the effectiveness of sawtooth serrations at high frequencies is overpredicted by using the frozen turbulence assumption of Howe.

Another solution for trailing edge noise is to use optimised low-noise airfoils which are designed such that the boundary layer displacement thickness at the trailing edge, δ^*, is reduced while maintaining aerodynamic performance, see also Eq. 1.4. In the study by Oerlemans et al. (2009) field measurements were performed on a full scale wind turbine with one standard blade, one blade with sawtooth trailing edge serrations, and one blade with an optimised airfoil shape. A large horizontal microphone array was used to locate and quantify the noise of the individual blades. The results showed that both the optimised airfoil blade and the serrations blade reduced the trailing edge noise at low frequencies compared to the standard blade. The sawtooth serrated blade obtained an average overall noise reduction of 3.2 dB compared to 0.5 dB for the optimised airfoil blade. This suggests that trailing edge serrations are a better way to mitigate trailing edge noise than optimised low-noise airfoils.

Another way to reduce the boundary layer displacement thickness at the trailing edge is by using an active flow control system, for example suction or blowing through the airfoil surface. Although this might be an effective solution to reduce trailing edge noise these type of solution is likely to be complex. Furthermore, the active systems that are used for the suction or blowing often produce noise as well making them unfavourable for noise reduction.

A different trailing edge add-on for noise reduction is the attachment of trailing edge brushes, which consist of closely spaced (flexible) fibers. The mechanism for the noise reduction might be due to the porous nature of the brushes which dampens the turbulent fluctuations in the boundary layer that cause trailing edge noise. An alternative explanation might be that the sudden impedance mismatch at the sharp trailing edge is replaced by a more gradual change in impedance over the brush extensions (Barone (2011)).

Herr and Dobrzynski (2005) used several trailing edge brushes on a flat plate geometry with a blunt trailing edge for a chord-based Reynolds number of $2.1 \times 10^6 - 7.9 \times 10^6$. The results showed a potential noise reductions in excess of 10 dB. However, due to the blunt trailing edge, vortex shedding noise was present which is not expected for sharp trailing edge airfoils, making it less applicable in this case. Further experiments of Herr (2007) on a NACA 0012 wing, showed a noise reduction from 5 dB to 10 dB at zero angle of attack for a small trailing edge thickness. According to Herr and Dobrzynski (2005) trailing edge vortex shedding noise was the key component in the noise generation. For sharp trailing edges the effectiveness of trailing edge brushes in reducing noise is an open question, therefore brushes are not further examined in the current study.

A similar concept to replace the impedance discontinuity at the trailing edge by a more gradual change in impedance is the use of a porous trailing edge. In the studies by Geyer et al. (2009, 2010) trailing edge noise has been measured for different tripped airfoils with entirely porous surfaces at low Mach ($M = 0.07 - 0.14$) and Reynolds number ($Re = 4 \times 10^5 - 8 \times 10^5$).

Depending on the permeability of the surfaces a sound reduction was found up to 10 dB compared to the non-porous airfoils for low and medium frequencies, and more noise was produced at high frequencies. However, the aerodynamic performance of the airfoils suffered with increasing permeability compared to the baseline airfoil. A significant loss of lift and increase of drag was measured for all porous airfoils, suggesting that porous wings might not be suited for energy generation.

As mentioned above several potential solutions exist to reduce trailing edge noise. However, multiple studies show that trailing edge serrations seem most effective (e.g. Howe (1991a,b); Oerlemans et al. (2009); Gruber et al. (2010)). However clear understanding of the mechanisms behind noise reduction using serrations is sparsely present and sometimes contradicting.

1.3 Research objectives

In order to get a better understanding of the mechanism involved, a link between the three-dimensional flow field and acoustic field has to be made. This can be done experimentally by using particle image velocimetry (PIV) and a microphone array system in a wind tunnel.

PIV has the drawback that the flow near the body, the inner layer of the boundary layer, cannot be captured. In order to get a good resolution the field of view is often limited to a portion of the flow which makes a complete analysis of the wing time-consuming.

In many PIV studies the flow speed for the wind tunnel is limited by the acquisition frequency of the camera. If the flow velocity is too high the distance the particles move between two frames taken by the camera becomes so large that the images cannot be correlated accordingly, resulting in a loss of information. The sound generation measurements, however, require a minimum flow velocity. Below a certain velocity the background noise is on the same order of the airfoil trailing edge noise, resulting in a low signal-to-noise ratio, making noise qualification and quantification troublesome. This different flow velocity limits can result in the decoupling of measurements, the flow dynamics should be captured at a different velocity than the noise characteristics of the wing. This is for example the case in the study by Avallone et al. (2016), where the flow measurements are taken at 10 m/s and the sound measurements at 30 m/s freestream velocity. This makes understanding the mechanism of flow induced sound difficult. Considering these limitations the computational approach might be the best method for the analysis.

The goal of this research is to reduce trailing edge noise for large wind turbines. Trailing edge serrations seem to be a good method for noise source reduction, however optimisation of these add-ons require a deeper understanding of the physics behind trailing edge noise.

Therefore the research objective is to analyse trailing edge noise source generation and propagation to aid the development for improved trailing edge serrations for trailing edge noise reduction, by using numerical simulations. To achieve this, the following research question and sub-questions are posed:

How do trailing edge serrations reduce the noise generated by wings?

1. How to accurately simulate the flow and acoustics around a wing with the computational resources available?
    - What mesh is most suited for the aeroacoustic simulations?
    - What methods can be used to calculate the near and far field acoustics, and what are their differences?
    - What are the differences for the flow and acoustic field between the simulation and the analytical/experimental reference solutions?
2. What is the difference in flow topology around a wing with and without serrations?.
3. What is the mechanism behind noise reduction for a wing with serrations?

1.4 Outline of thesis

To answer the research questions computational simulations will be performed on a unserrated and serrated NACA 0018 wing. In order to understand the phenomena in detail, the simulations need to resemble reality, ideally. Therefore, turbulence modelling is eliminated by using a direct numerical simulation. The aeroacoustic simulations will be performed using the commercial software package Exa PowerFLOW 5.1b and PowerACOUSTICS 3.1b. An explanation of the computational methodology involved, is presented in Chapter 2 after which the analysis on a clean (unserrated) NACA 0018 wing is presented in Chapter 3. Next, the serrated NACA 0018 wing is analysed and compared with the unserrated case in Chapter 4. At last conclusions of this thesis are presented, together with recommendations for future work.

Chapter 2

Computational methodology

As presented in the previous chapter the aeroacoustic analysis will be performed using the Lattice Boltzmann Method incorporated in PowerFLOW. In this chapter, first, the Lattice Boltzmann method will be explained in more detail, after which the acoustic models used in this thesis are presented.

2.1 Fluid model

Several attempts have been made to investigate the flow and acoustics related to airfoil self-noise using computational fluid dynamics (CFD). In Tab. 2.1 a brief, and incomplete, overview of several recent studies regarding trailing edge noise is given, with the corresponding method and application.

Article	Method	Re	Turbulence model	Application
van der Velden et al. (2016)	LBM	2.65×10^5	LES	NACA 0018
Sanjosé et al. (2014)	LBM	1.5×10^5	DNS	CD airfoil
Sanjosé and Moreau (2011)	LBM	1.5×10^5	DNS	CD airfoil
Sandberg and Jones (2011)	NS	5×10^4	DNS	NACA 0012
Winkler et al. (2011)	NS	1.9×10^5	LES	NACA 6512-63
Christophe et al. (2010)	NS	1.6×10^5	LES	CD airfoil
Wang and Moin (2000)	NS	2.15×10^6	LES	Bevelled plate
Mathey (2008)	NS	1.8×10^5	RANS-LES	Bevelled plate
Kim et al. (2006)	NS	1.6×10^5	LES	NACA 0018

Table 2.1: Previous aeroacoustic simulations related to wing self-noise.

The classical Navier-Stokes (NS) method is used frequently to simulate aeroacoustic problems. Recently, however, a shift is being made to the Lattice Boltzmann method. For example the second AIAA workshop on Benchmark problems for Airframe Noise Computations (BANC-

II) about landing gear noise (Sesor et al. (2004); Lew et al. (2007); Nölting et al. (2010); Casalino et al. (2013); Brionnaud et al. (2016)). The LBM offers significant advantages in terms of integration time and scalability due to a simpler partial differential equations system compared to traditional Navier-Stokes methods (Sanjosé and Moreau (2011)). Also, the LBM can simulate compressible flows which makes aeroacoustic analysis possible. Due to these features of the Lattice Boltzmann method and the fact that it can simulate at high Reynolds numbers it is a good method for the aeroacoustic analysis in this thesis.

2.1.1 Lattice Boltzmann Method

The Lattice Boltzmann method originates from the Lattice Gas Automata (LGA) method and is a simplified version of the continuous Boltzmann equation. In the full Boltzmann equation individual particles in the fluid are the subject of interest. These particles are free to move and collide with each other on account of kinetic equations, that are continuous in space and time. The Lattice Boltzmann method is produced to incorporate the essential physics of the microscopic or mesoscopic processes that cause the macroscopic averaged properties of the flow, like pressure and velocity, to follow the desired macroscopic equations (Chen and Doolen (1998)). The LBM uses groups of particles with a certain distribution function that are allowed to move in a limited number of directions between lattice nodes. When two or more particle groups are positioned at the same node they collide with each other and move further according to a collision model. An example of the discrete velocities for a two-dimensional lattice grid is presented in Fig. 2.1.

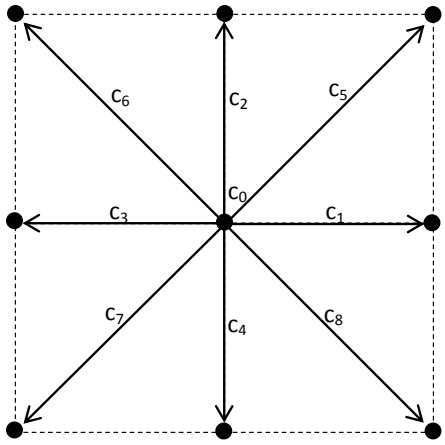

Figure 2.1: Example of the discrete velocities for a two-dimensional lattice.

The groups of particles in the LBM go through two different phases in each time step of the simulation. First the particles move from one node to another, which is the movement phase. If after this movement several groups of particles occupy the same lattice node, a collision phase will be activated. A collision model is used to conserve the total mass, momentum and energy in the node while changing the speed and direction of the particles. The particle

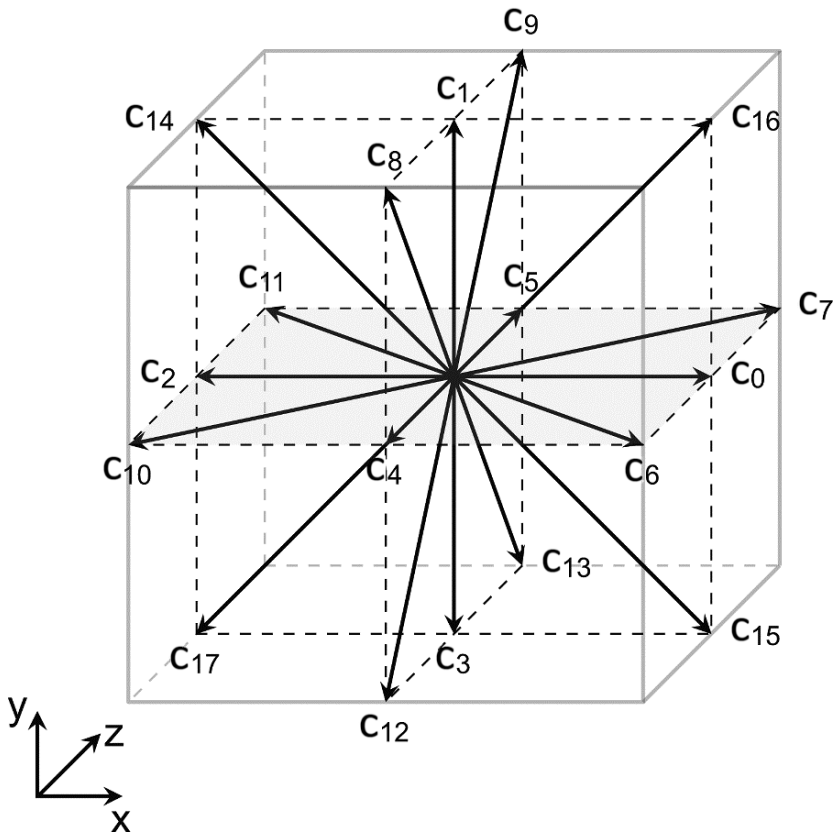

Figure 2.2: Example of the discrete velocities for a three-dimensional lattice. Adapted from Schneider et al. (2015).

movement and collision is illustrated in Fig. 2.3 for a two-dimensional lattice grid. Although the individual particle distributions can move only in discrete directions and speeds, the macroscopic fluid velocity can be continuous in value and direction.

The movement and collision phases are governed by the following equation, expressed in non-dimensional lattice units, which describes the evolution of the particle distribution function with time.

$$f_i(\mathbf{x} + \mathbf{c}_i \Delta t, t + \Delta t) = f_i(\mathbf{x}, t) + \Omega_i(f(\mathbf{x}, t)), \qquad (i = 0, 1, ..., m) \tag{2.1}$$

Where f_i is the particle distribution function in the direction i, $\mathbf{x}$ the lattice node position, $\mathbf{c}_i$ the discrete velocity vector in the ith direction, and Δt the time step increment. The operator Ω_i represents the rate of change of the particle distribution function due to collision.

Several different collision operators exist for the lattice Boltzmann method and can be found in the book of Succi (2001) about the Lattice Boltzmann equation. Different codes that have incorporated the lattice Boltzmann method have different collision operators. Because PowerFLOW 5.1b is used for the simulations in this thesis only the collision model implemented in this package will be explained in the following section.

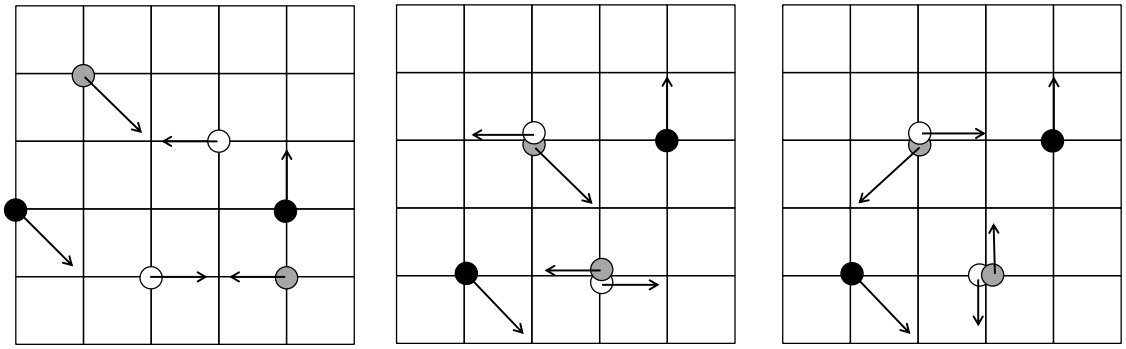

(a) Movement phase

(b) After movement before collision

(c) After collision

Figure 2.3: Movement and collision phase example for a two-dimensional lattice grid

2.1.2 Collision model: Bhatnagar-Gross-Krook

As mentioned above the collision model implemented in PowerFLOW 5.1b is the only one being discussed in this thesis. Note, the variables in the following equations are dimensionless quantities used by the solver, unless otherwise stated. The collision model of interest is the Bhatnagar-Gross-Krook (BGK) operator by Bhatnagar et al. (1954), which also is the most common form:

$$\Omega_i = -\frac{\Delta t}{\tau}\left[f_i(\mathbf{x},t) - f_i^{eq}(\mathbf{x},t)\right] \tag{2.2}$$

In this collision term, τ represents the relaxation time parameter and f_i^{eq} the distribution function at local equilibrium, which depends on local fluctuating properties. f_i^{eq} is derived from the Maxwell-Boltzmann distribution function under the constraints that conservation of mass and momentum are satisfied, so that the Navier-Stokes equations are recovered. The derivation for this distribution function at local equilibrium can be found in He and Luo (1997). For an isothermal fluid it is defined as:

$$f_i^{eq} = \rho\omega_i\left\{1 + \frac{\mathbf{c}_i\cdot\mathbf{u}}{{c_s}^2} + \frac{(\mathbf{c}_i\cdot\mathbf{u})^2}{2{c_s}^4} - \frac{\mathbf{u}^2}{2{c_s}^2}\right\}, \tag{2.3}$$

where ρ and $\mathbf{u}$ are the macroscopic density and velocity, respectively, ω_i the weights corresponding to the lattice velocity vectors $\mathbf{c}_i$, and c_s is the speed of sound of the lattice system equal to $c_s = 1/\sqrt{3}$. The physical speed of sound C_s is related to the local physical voxel size Δx_{phys} and time step according to:

$$C_s = c_s\frac{\Delta x_{phys}}{\Delta t_{phys}}. \tag{2.4}$$

The single relaxation time, τ, is related to the dimensionless kinematic viscosity (Chen and Doolen (1998)):

$$\nu = {c_s}^2 \left(\frac{\tau}{\Delta t} - \frac{1}{2} \right), \tag{2.5}$$

According to Chen et al. (1992) $\tau/\Delta t$ should generally be larger than a half for numerical stability. The equation of state for an ideal gas is incorporated in the model, relating the macroscopic pressure (p) with the speed of sound:

$$p = \rho {c_s}^2. \tag{2.6}$$

The macroscopic fluid properties ρ and $\mathbf{u}$ are related to the particle distribution function according to the hydrodynamic moments:

$$\rho = \sum_{i=0}^{m-1} f_i, \qquad \rho\mathbf{u} = \sum_{i=0}^{m-1} f_i \mathbf{c}_i, \tag{2.7}$$

The weights corresponding to the discrete velocity vectors are dependent on the type of lattice structure and are listed in Tab. 2.2 acquired from Aidun and Clausen (2010) for the most popular velocity sets, referred to as DnQm. Where the first part Dn refers to the dimensionality and the second part Qm to the total number of discrete velocity vectors.

ω_i	No. (2D)	$\lvert c_i \rvert$	D2Q9	D3Q15	D3Q19	D3Q27
ω_0	1	0	4/9	2/9	1/3	8/27
ω_1	6 (4)	1	1/9	1/9	1/18	2/27
$\omega_{\sqrt{2}}$	12 (4)	$\sqrt{2}$	1/36	0	1/36	1/54
$\omega_{\sqrt{3}}$	8 (0)	$\sqrt{3}$	0	1/72	0	1/216

Table 2.2: The magnitude and the number of velocity vectors for lattice models D3Q15, D3Q19, and D3Q27 and the corresponding weights ω_i (Aidun and Clausen (2010)).

The Lattice Boltzmann method implemented in the software uses non-dimensionalised variables in the equation. The parameters in the Lattice Boltzmann equation are given in terms of lattice units. The time step, lattice spacing and lattice density are used for the time, length and density/mass units. The lattice units are implemented in the following scales for non-dimensionalisation (Aidun and Clausen (2010)):

$$\left.\begin{array}{ll} \text{Characteristic length scale} & L_s \\ \text{Characteristic velocity} & U_s \\ \text{Reference density} & \rho_s \end{array}\right\}. \tag{2.8}$$

Using these characteristic scales the non-dimensional macroscopic parameters, which are of interest become:

$$\left.\begin{array}{ll} \text{Time} & \hat{t} = \frac{tU_s}{L_s} \\ \text{Length} & \hat{\mathbf{r}} = \frac{\mathbf{r}}{L_s} \\ \text{Density} & \hat{\rho} = \frac{\rho}{\rho_s} \\ \text{Macroscopic velocity} & \hat{\mathbf{u}} = \frac{\mathbf{u}}{U_s} \\ \text{Reynolds number} & Re = \frac{U_s L_s}{\nu} \end{array}\right\}. \tag{2.9}$$

The Courant-Friedrichs-Lewy (CFL) number of the Lattice Boltzmann method is defined using lattice units as (Huang et al. (2015)):

$$CFL = \frac{c_i \Delta t}{\Delta x_i}, \tag{2.10}$$

where $\Delta t = 1$ *timestep* in lattice units and Δx_i the distance between two lattice points in direction i for a unit lattice size (corresponding to the smallest voxel size). As can be seen from this definition, the CFL number is exactly equal to unity. This value is constant throughout the domain for varying voxel sizes. Due to the explicitness of the LBM scheme the time step size can be increased with voxel size, to accommodate a CFL number of 1. As the size of voxels is increasing in factors of two, the local time step is also increased in factors of two. Due to this difference in time stepping, larger voxels will not be evaluated at every time step of the smallest cells. To get an idea of the computational cost of a certain mesh a time step equivalent number of voxels is introduced. This time step equivalent number of voxels is the sum of the number of voxels (N) scaled to the operation of the shortest time step:

$$\begin{aligned} \#\ of\ Fine\ Equivalent\ Voxels = {} & N(finest\ scale) + N(2nd\ finest\ scale)/2 \\ & + N(3rd\ finest\ scale)/4 + ... + N(coarsest)/(2^{(number\ of\ grid\ levels-1)}). \end{aligned} \tag{2.11}$$

Due to the fact that DNS computations will be done no turbulence modelling is involved. The turbulence modelling in the LBM is therefore not further discussed in this thesis.

2.2 Acoustic model

Now that the fluid model is described- a more in depth view on the acoustic modelling is presented in this section. At first a general overview of aeroacoustics (in the LBM) is given, after which the different applied acoustic models will be presented.

Computational aeroacoustics (CAA) can be split up in two main fields, a direct noise computation and hybrid approaches. In direct noise computation (DNC) the unsteady flow field and the acoustics are simulated in a coupled fashion for the entire domain; the acoustics and flow field are calculated simultaneously. This DNC can be achieved by using a large eddy simulation (LES) or a direct numerical simulation (DNS) for a compressible fluid. In a DNS the entire range of scales of the flow (and sound) is calculated where for a large eddy simulation a subgrid-scale model is used for the smallest scales of aerodynamic motion, so that the computational load is reduced.
For aerodynamic problems, ignoring sound, the smallest turbulence scale is the Kolmogorov

scale η and the largest is in the order of the characteristic body length L. The size of acoustic fluctuations is characterised by the wavelength λ, which is typically much larger than η. In order to accurately capture the turbulent motion in the vicinity of the wing the cell size should be of the order of the Kolmogorov scale which results in a really fine mesh and therefore a high computational load.
The Kolmogorov length η scales with the Reynolds number as follows, see Pope (2000):

$$\eta \sim l_0 \mathcal{R}e^{-3/4} \tag{2.12}$$

Where l_0 is the scale of the largest eddies which is comparable with the characteristic flow length scale L. The maximum cell size is therefore limited to the Reynolds number. For a three-dimensional domain the number of cells N required in the vicinity of the wing becomes:

$$N \sim \left(\frac{L}{\eta}\right)^3 \sim \mathcal{R}e^{9/4} \tag{2.13}$$

As can be seen from the equation above, increasing the Reynolds number will result in a large increase in the number of cells, and so the computational load. For regions far away from the source region (away from the body and wake) the size of the turbulent eddies increase in size and become larger than the acoustic length scale, λ. At this far field region the cell size is limited by the acoustic wavelength, resulting in a much finer mesh then is needed typically for purely aerodynamic simulations (de Roeck (2007)).

In contrast with DNC, the hybrid methods do not aim to capture the far field radiated sound directly but use other methods for predicting the acoustic propagation. The noise generating mechanisms behave differently than the sound wave propagation which allows for the entire domain to be decomposed into different zones or regions. Each zone or region can be solved on a different mesh using different numerical techniques, which can reduce the computational load drastically. Due to the fact that DNC for the entire field is too computationally expensive, three different methods for sound extraction are used in this thesis, which will be explained in the following section.

2.2.1 Aeroacoustics and the LBM

As said in the previous section the length scales involved with aeroacoustics are in a broad region for DNC. Not only do length scales differ between the aerodynamic flow and acoustics in the far field, also the energy levels between the two field differ a lot. Typically the velocity fluctuations for acoustics is of the order of 10^3 to 10^4 times smaller than the aerodynamic velocity fluctuations. Because the length and energy scale separation between the acoustic and aerodynamic field is large a low-dispersive and a low-dissipative numerical scheme is required to preserve the acoustic waves correctly (Li et al. (2006b)). In order the achieve this low dispersion and dissipation errors accurate high-order schemes are needed for the classical NS method according to Tam (2004).

Marié et al. (2009) compared the performance of the classical high-order schemes for NS with the Lattice Boltzmann method to see whether the LBM has the required properties

to model aeroacoustics. In this comprehensive study several forms of the LBM have been analysed, including the most common BGK-model, on which PowerFLOW is based. Using a von Neumann stability analysis, the dispersion and dissipation of the different schemes were compared.

The analysis between the multiple relaxation time (MRT) model and the BGK-model has highlighted that the dispersion error is similar while the dissipation of the acoustic modes is higher for the MRT model compared to the BGK model, making BGK better for aeroacoustic simulations. Comparing the dispersion and dissipation errors of the LBM BGK scheme and the high-order NS schemes, Marié et al. (2009) found that the LBM has low dissipative capabilities compared to the optimised high-order NS schemes, and that the LBM is faster for a given dispersion error, giving the Boltzmann method intrinsic aeroacoustic capabilities.

Another study about the use of the LBM for aeroacouastics is performed by Li et al. (2006a). The LBM was compared with the classical DNS approach using the Navier-Stokes equations for three different two-dimensional test cases. The tests showed that the results of the simulations were identical. This suggests that the LBM is an alternative for simulations of aeroacoustic problems.

The LBM has been used in aeroacoustic studies, for example by Sanjosé & Moreau. Sanjosé and Moreau (2011) performed a DNS using the LBM on a controlled diffusion airfoil to examine the trailing edge noise for a chord based Reynolds number of 150,000. This study is the first attempt at computing the trailing edge noise of the CD airfoil directly at such high Reynolds number, by using the LBM (Sanjosé and Moreau (2011)). For their analysis use has been made of the commercial software Exa PowerFLOW®. The simulation consisted of a three-dimensional mesh of 640 million voxels which ran on 512 processors Intel Xeon X5560 2.80GHz for 170 hours for 10 flow passes. Due to the limited computational resources available for the current thesis it is unexpected that a simulations with similar Reynolds number can be achieved.

For DNC the assumptions made for the turbulent field due to turbulence modelling often prohibit accurate acoustic results de Roeck (2007). The aim of this thesis is to get a better insight into the mechanism behind trailing edge noise so an accurate acoustic field is preferred. Therefore this would make LES less favourable than DNS for this study.

2.2.2 Acoustic propagation models

In this study three different techniques will be used to gather the acoustics from the simulations. Due to the fact that the LBM is inherently compressible and provides transient solutions, the sound pressure field can be extracted directly from the flow by probes. Apart from obtaining the sound pressure field directly several hybrid methods exist to compute the far field noise predictions, which are explained next.

The so-called hybrid methods consist of a two-step approach. The (aero)acoustic sources are obtained by computations and an analytical analogy is used to calculate the far-field

spectrum. The main advantage with this approach is that the requirements for the mesh at the far-field are less stringent, and only the sources need to be accurately captured.

Lighthill equation

The first acoustic analogy was derived by Lighthill (1952) and forms the basis of the two analogies used in this thesis. Lighthill reformulated the NS equations to come up with a variation of the acoustic wave equation:

$$\frac{\partial^2 \rho'}{\partial t^2} - a_0^2 \nabla^2 \rho' = \frac{\partial^2 T_{ij}}{\partial x_i \partial x_j}, \tag{2.14}$$

where a_0 is the speed of sound in the medium, ρ' is the density relative to the density at rest (ρ_0), and T_{ij} is the Lighthill stress tensor. This tensor can be expressed as:

$$T_{ij} = \rho u_i u_j + [(p - p_0) - a_0^2(\rho - \rho_0)]\delta_{ij} + \tau_{ij}, \tag{2.15}$$

where u is the flow velocity, p is the pressure, p_0 is the pressure at rest, δ_{ij} is the Kronecker delta, and τ_{ij} is the viscous stress tensor. The source term on the right-hand side of Eq. 2.14 is generally computed using flow simulations, while the transport of density variations is represented by the left-hand side. The density fluctuations are related to the pressure by the equation of state:

$$\rho' = \frac{p'}{a_0^2} \tag{2.16}$$

At low Mach number isotropic flows the viscous stresses in T_{ij} are assumed to be negligible, providing that any difference in temperature between the flow and the outside (uniform) air is due to kinetic heating or cooling Lighthill (1952). Due to this T_{ij} reduces to:

$$T_{ij} \approx \rho_0 u_i u_j. \tag{2.17}$$

The general solution of Eq. 2.14 by Lighthill (1952) is:

$$p' = \frac{1}{4\pi a_0^2} \frac{\partial^2}{\partial x_i \partial x_j} \int_V \frac{T_{ij}\left(\mathbf{y}, t - \frac{|\mathbf{x}-\mathbf{y}|}{a_0}\right)}{|\mathbf{x}-\mathbf{y}|} d^3\mathbf{y}, \tag{2.18}$$

where $\mathbf{x}$ is the distance between the origin and the observer (outside the source region) and $\mathbf{y}$ is the distance between the origin and the noise source.

Lighthill's analogy does not take solid boundaries or moving objects into account, making it solely applicable on sound generated by free turbulence. This limits its direct use for this thesis. However, several extensions to the original Lighthill equation exist which do account for these. The analogy of Curle (1955) accounts for solid boundaries and the formulation by Ffowcs Williams and Hawkings (1969) additionally accounts for movement of these boundaries.

Curle's analogy

Fixed, rigid object can produce sound when interacting with flow turbulence. Instead of the free field quadrupole volume sources of Lighthill (1952), this interaction creates surface dipole sources.

The analogy of Curle (1955) consists of a similar equation as the one from Lighthill with the addition of a surface pressure term.

The resulting general solution of Curle is:

$$p' = \frac{1}{4\pi a_0^2}\frac{\partial^2}{\partial x_i \partial x_j}\int_V \frac{T_{ij}\left(\mathbf{y}, t - \frac{|\mathbf{x}-\mathbf{y}|}{a_0}\right)}{|\mathbf{x}-\mathbf{y}|}\mathrm{d}^3\mathbf{y} - \frac{1}{4\pi a_0^2}\frac{\partial}{\partial x_i}\int_S \frac{p_{ij}\mathbf{n_i}\left(\mathbf{y}, t - \frac{|\mathbf{x}-\mathbf{y}|}{a_0}\right)}{|\mathbf{x}-\mathbf{y}|}\mathrm{d}S(\mathbf{y}), \tag{2.19}$$

where $p_{ij} = p'\delta_{ij} + \tau_{ij}$ and n_i is the outward normal from the fluid.

Ffowcs Williams-Hawkings analogy

The most general form of Lighthill's analogy is the Ffowcs Williams and Hawkings (1969) analogy. In addition to the analogy of Curle (1955) the Ffowcs William-Hawking (FW-H) analogy accounts for the movement of solid surfaces.

$$\frac{\partial^2 \rho'}{\partial t^2} - a_0^2\nabla^2\rho' = \underbrace{\frac{\partial^2 T_{ij}}{\partial x_i \partial x_j}}_{\text{Quadrupole}} - \underbrace{\frac{\partial}{\partial x_i}\left(p_{ij}\delta(f)\frac{\partial f}{\partial x_j}\right)}_{\text{Dipole}} + \underbrace{\frac{\partial}{\partial t}\left(\rho_0 v_i \delta(f)\frac{\partial f}{\partial x_i}\right)}_{\text{Monopole}}, \tag{2.20}$$

where $p_{ij} = p'\delta_{ij} + \tau_{ij}$ and $\delta(f)$ is the Dirac delta function.

From the equation it can be seen that additional dipole and monopole sources are incorporated for the stationary surfaces and moving surfaces respectively. The general solution to this equation was found by Ffowcs Williams and Hawkings (1969):

$$\begin{aligned} p' =& \frac{1}{4\pi a_0^2}\frac{\partial^2}{\partial x_i \partial x_j}\int_V \frac{T_{ij}\left(\mathbf{y}, t - \frac{|\mathbf{x}-\mathbf{y}|}{a_0}\right)}{|\mathbf{x}-\mathbf{y}|}\mathrm{d}^3\mathbf{y} - \frac{1}{4\pi a_0^2}\frac{\partial}{\partial x_i}\int_S \frac{p_{ij}\mathbf{n_i}\left(\mathbf{y}, t - \frac{|\mathbf{x}-\mathbf{y}|}{a_0}\right)}{|\mathbf{x}-\mathbf{y}|}\mathrm{d}S(\mathbf{y}) \\ &+ \frac{\partial}{\partial t}\int_S \frac{\rho_0 v_n\left(\mathbf{y}, t - \frac{|\mathbf{x}-\mathbf{y}|}{a_0}\right)}{|\mathbf{x}-\mathbf{y}|}\mathrm{d}S(\mathbf{y}), \end{aligned} \tag{2.21}$$

The implementation of the time-domain Ffowcs Williams and Hawkings (1969)(FW-H) formulation is developed by Farassat and Succi (1983) and is known as formulation 1A and is extended by Brès et al. (2010) based on the convective form of the FW-H equation. This is the form used by PowerFLOW and also applied in this thesis.

Time-dependent flow field on a surface mesh is used as an input to the FW-H solver to retrieve the far-field noise spectra. This surface mesh is either defined as a solid surface corresponding to the wing (further denoted as the analogy of Curle) or a permeable surface surrounding the wing and part of the wake (further denoted as FW-H analogy) For both the Curle analogy and the FW-H analogy the radial distance $|\mathbf{x} - \mathbf{y}|$ is set to 10 times the chord length, which is assumed to be far enough in the far-field. Due to the different radial distances between the direct probes and the analogies the results will later be scaled to compare the noise data with the near field results.

Chapter 3

Clean wing analysis

3.1 Computational setup

In order to simulate the flow and sound as accurate as possible (underresolved) direct numerical simulations are performed to limit the modelling of turbulence. Ideally the experiments done by Avallone et al. (2016); Arce Léon et al. (2016a) are simulated at the same inflow conditions to validate PowerFLOW by direct comparison. However, due to the grid resolution required for DNS simulations this would result in enormous meshes and excessive computation times.

The PIV experiments by Arce Léon et al. (2016a) were done on a 200 mm chord NACA-0018 wing section with an incoming flow velocity of 20 m/s which corresponds to a chord-based Reynolds number of around $\mathcal{R}e_c = 2.6 \times 10^5$ and a Mach number of $M = 0.058$.

As an indication of the mesh size for a simulation of the experiment a case was made with PowerFLOW. This case considered of a 40 mm span ($= \frac{1}{5}c$) wing section at $\mathcal{R}e_c = 2.6 \times 10^5$ and $M = 0.31$. This Mach number is chosen by PowerFLOW to make the mesh requirements less stringent. Ideally the difference between the experimental Mach number and the simulated Mach number is kept to a minimum as sound scattering largely depends on the Mach number, see Chapter 2. The mesh corresponding to this case consisted of 691 million fine equivalent voxels (1.47×10^9 voxels total). The predicted simulation time by PowerFLOW on 80 Linux Xeon E5 2.9 GHz processors per time step was 1.32 seconds, resulting in an estimated total run time for a coarsened mesh of around 16 days for 0.4 seconds of simulated time (1.1M time steps). Ideally the total run time of a simulation is in the order of a few days to make testing PowerFLOW to changes in the input and setup less intensive.

In order to reduce the computation time of the aeroacoustic simulations the Reynolds number has been lowered to $Re_c = 40,000$. Instead of decreasing the incoming flow velocity to adapt the Reynolds number the kinematic viscosity ν has been scaled.

The size of the smallest voxels is related to to the smallest scales of turbulence, which are determined by the Reynolds number. In order to achieve the physical speed of sound in Eq. 2.4, the physical time step size is also determined indirectly by the Reynolds number. If the flow velocity was decreased by a factor the total simulated time should be increased by the same factor in order to achieve the same number of flow passes along the airfoil to acquire a sufficient sample time for the averaging, making the reduction in Reynolds number less effective. The free stream velocity has been increased to keep the scaling of the kinematic viscosity around a factor 13. The flow conditions used in the simulations are a free stream velocity of 40 m/s and a Mach number of $M = 0.116$.

To further reduce the computational load the span of the wing has been reduced 20 mm corresponding to one-tenth of the chord. Ideally a span of around $\frac{1}{5}c$ is simulated, as in Sandberg and Jones (2011); Jones and Sandberg (2012, 2010). However, this could not be achieved with the computational resources available, for a reasonable computational time. In Sanjosé et al. (2014) a similar spanwise length of $\frac{1}{9}c$ was successfully used to simulate the flow around a serrated controlled-diffusion airfoil. Although the spanwise length is slightly smaller compared to Sanjosé et al. (2014) it is far from the limited span used in Wang and Moin (2000) where they simulated a span of $\frac{1}{47}c$ for a bevelled trailing edge plate. Wang and Moin (2000) showed that the spanwise length was insufficient and suggested to use a wider computational domain.

In order to achieve a turbulent boundary layer across the wing trailing edge for such low Reynolds number zig-zag strips were installed on the airfoil surface. Boundary layer tripping was found to be very sensitive. Several trip heights and trip locations were tested. After several attempts the traditional method of boundary layer tripping was skipped. Instead of tripping the boundary layer on a fully no-slip wall wing surface the same strategy as applied by de Jong (2012) was used.

The NACA 0018 wing is split chordwise in two different sections. The front part which covers 20% of the wing is set as a frictionless wall, where the back 80% of the wing is set as a no-slip wall. The trip is located just after 20% chord, close to the intersection of the two different sections. A side view with the different sections of the NACA 0018 model is presented in Fig. 3.1.

Transition on the pressure and suction sides is enforced by zig-zag strips of 1 mm height ($h_{trip} = 0.005c$) and 3 mm length ($l_{trip} = 0.015c$). One zig-zag strip spans 2.2 mm ($s_{trip} = 0.011c$), resulting in 9 triangle shapes in a repetitive pattern. A more detailed view of the transition trips is presented in the top right corner of Fig. 3.1.

The computational setup consist of a NACA 0018 wing of 200 mm chord and 20 mm span centred in a domain of 12 chords in length and height. Different volumes of refinement (VRs) are surrounding the body with the finest cells located at the inner boundary layer and the trips ,while the coarsest cells are near the domain boundary. The refinement zones are ranked from coarsest (VR 0) to finest (VR 7), where grid size changes by a factor 2 for adjacent regions. In Fig. 3.2 an side view of the computational domain with the different refinement zones is presented. From this figure you can see that there are 4 cylindrical refinement zones with a radius of 2, 3, 4 and 5 chords, respectively. The green domain, the funnel, surrounding

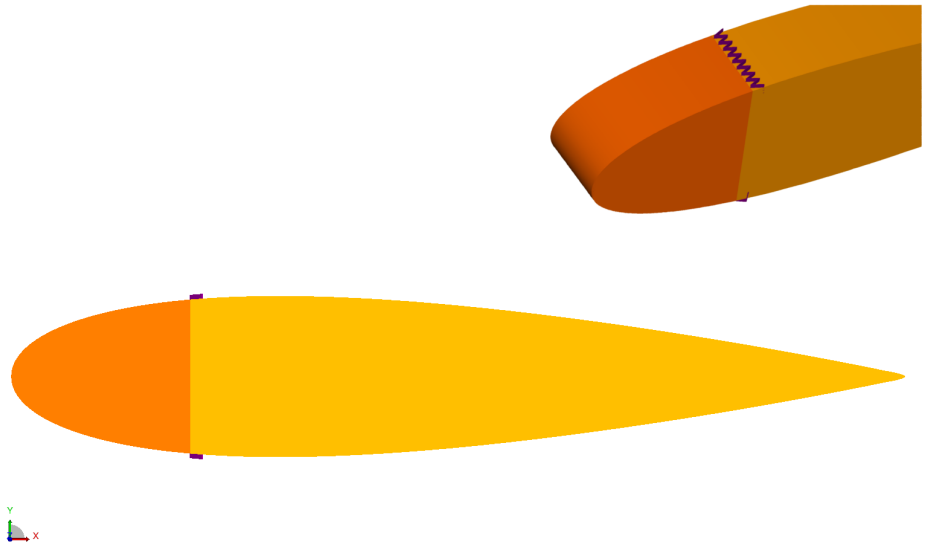

Figure 3.1: Side view and isometric view of the NACA 0018 wing with the different sections (orange: frictionless wall and yellow: no-slip wall) and the trips (in purple).

the wing and a large part of the wake is used to recover the far field acoustics using Ffowcs Williams and Hawkings (1969) equation. This funnel is a permeable surface on which the time-dependent flow field variables, i.e. pressure and velocity, are captured to use in the analogy.

A close-up of the VRs around around the wing is also shown in Fig. 3.2. Two different offsets around the wing of 2 mm and 20 mm respectively can be observed. Also downstream of the wing a zone is refined to capture part of the wake, to compare later with the serrated wing case.

For the validation of PowerFLOW three different meshes are used to compute the flow field and acoustic characteristics of the NACA 0018 wing. The coarsest mesh consists of 7 refinement zones for which the lower part of the boundary was resolved such that the real viscosity is achieved. For the intermediate and finest mesh the full boundary layer was resolved using a total of 8 refinement regions. The different meshes setups will be referred to as coarse, medium and fine in the remainder of this thesis.

The three meshes are identical in the regions further away from the airfoil. The refinement scales from the domain boundaries to the inner cylindrical VR are 0, 1, 2, 3 and 4 respectively. The voxel sizes corresponding to the different refinement scales are presented in Tab. 3.1.

For the coarse mesh the inner part (2 mm) of the boundary layer has a refinement scale of 6, which corresponds to a voxel size of 1.56×10^{-4} m or 6.4 $voxels/mm$. The outer part (up to 20 mm) of the boundary layer has VR scale 5, leading to a voxel size of 3.13×10^{-4} m or 3.2 $voxels/mm$. However, for refinement scales of 5 and below the solver is unable to achieve the desired viscosity, so it is locally increases the viscosity. For the medium mesh both the inner and outer part of the boundary layer have a refinement scale of 6, leading to the desired

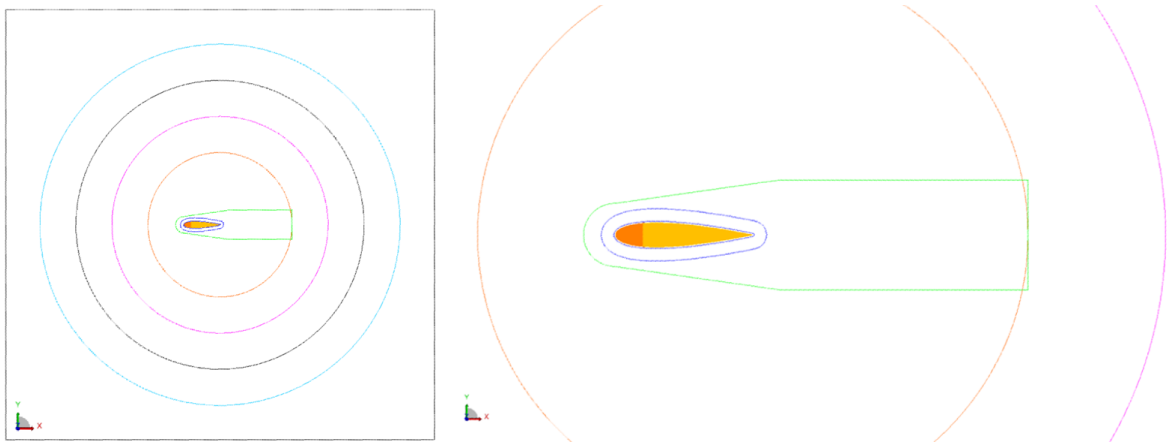

Figure 3.2: Side views of computational model. Colours indicate the boundaries of different refinement regions.

viscosity in the entire boundary layer. The desired viscosity is achieved in the fine mesh case by a refinement scale of 7 in the inner layer, corresponding to a voxel size of 7.81×10^{-5} m or 12.8 $voxels/mm$ and a refinement scale of 6 in the outer boundary layer. The difference of mesh refinement scales in the different mesh setups is also tabulated in Tab. 3.2. For direct numerical simulations in PowerFLOW the condition for the dimensionless wall distance is $y^+ \sim 1$. The meshes resulted in an average y^+ value over the back 80% of the airfoil (where surface friction exists) of 0.8 for the coarse and medium mesh, and 0.4 for the fine mesh, respectively. This indicates that the inner boundary layer is meshed adequately.

VR scale	Voxel size $[m]$	Number of voxels / mm	Desired viscosity achieved
0	0.01	0.1	No
1	5×10^{-3}	0.2	No
2	2.5×10^{-3}	0.4	No
3	1.25×10^{-3}	0.8	No
4	6.25×10^{-4}	1.6	No
5	3.13×10^{-4}	3.2	No
6	1.56×10^{-4}	6.4	Yes
7	7.81×10^{-5}	12.8	Yes

Table 3.1: Voxel sizes for different refinement scales.

Mesh setup	Inner boundary layer	Outer boundary layer	Wake
Coarse	VR 6	VR 5	VR 5
Medium	VR 6	VR 6	VR 6
Fine	VR 7	VR 6	VR 6

Table 3.2: Difference of mesh refinement scales for the different mesh setups. See Tab. 3.1 for the corresponding voxel sizes.

The resulting coarse mesh consisted of approximately 68 million voxels or 24 million fine equivalent voxels. To simulate 0.25 seconds of simulation time a total of 943k time steps of 2.6×10^{-7} s were used. The simulation ran for approximately 1280 CPU hours on a

Linux Xeon E5-2690 2.9 GHz platform of 80 processors. The medium mesh consisted of approximately 216 million voxels or 90 million fine equivalent voxels. A total of 1886k time steps of 1.3×10^{-7} s were used. The simulation ran for approximately 7540 CPU hours. As the time step size is based on the smallest refinement scale the medium and fine mesh only differ in the number of voxels. The full mesh had approximately 246 million voxels or 122 million fine equivalent voxels. The simulation ran for approximately 12,070 CPU hours. The resulting mesh sizes are tabulated in Tab. 3.3

Mesh setup	Total No. of voxels $[\times 10^6]$	No. of fine equivalent voxels $[\times 10^6]$	No. of time steps $[\times 10^3]$
Coarse	68	24	943
Medium	217	90	1886
Fine	246	122	1886

Table 3.3: Number of voxels for the different mesh setups including the total number of time steps in the simulation.

In total 24 direct probes were placed in a circular pattern at a radial position of 1.5 chord lengths mid span around the wing trailing edge. The probes are located in the smallest cylindrical refinement zone, which is of VR scale 4. The probes are 1 voxel size large, which results in a size of 6.25×10^{-4} m. The maximum measurable frequency of the direct probes is limited by the local voxel size. To obtain sufficient accuracy for at least 12 cells per wavelength are necessary for the LBM (Habibi et al. (2013)). The expected frequency range is around 500 Hz - 5 kHz. To be save the cut-off frequency of 10 kHz is preferably achieved, which corresponds to a maximum voxel size at the probe location of 2.8 mm. Clearly the cut-off frequency is met by placing the direct probes at this position. Placement of the probes much further away (i.e. in the far-field) would result in stringent mesh requirements, making the simulations too computationally expensive.

All three simulations are run for a total of 0.25 seconds of simulation time (50 flow passes). Sampling started after reaching a steady transient solution, i.e. after 0.1 seconds of simulation time (20 flow passes). In the case setups the Mach number was set to same as experiment, to avoid the influence of Mach scaling. The fluid is isothermal with a temperature of $15°C$, resulting in a physical speed of sound of 340 m/s.

3.2 Results

The results for the straight trailing edge simulations are presented in this section. This section is split into two parts. First the results for the flow field are presented after which the acoustic emission results are shown.

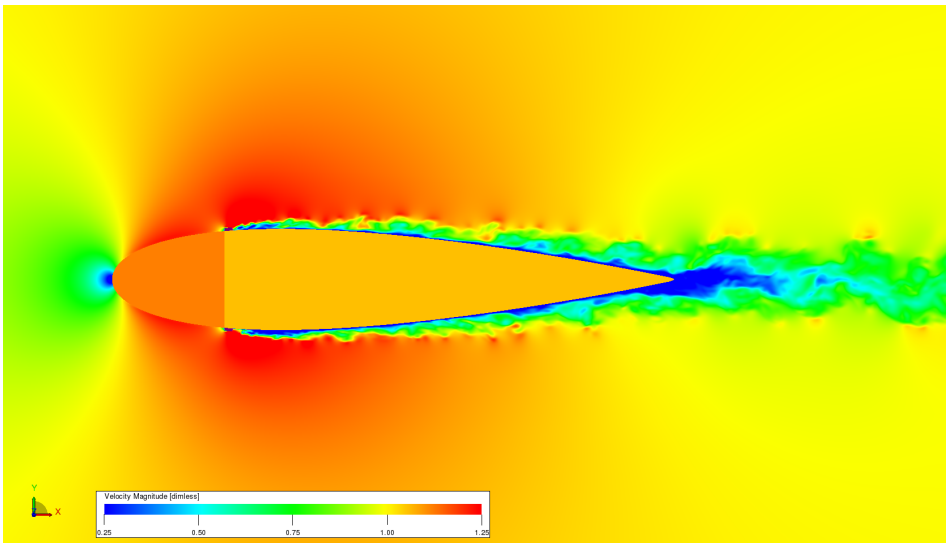

Figure 3.3: Instantaneous snapshot of the flow around the NACA 0018 wing coloured by the dimensionless velocity magnitude.

3.2.1 Flow field

In order to acquire any turbulent boundary layer trailing edge noise the flow has to be turbulent. As mentioned in Chapter 2 tripping the boundary layer was not trivial. However, using the frictionless wall condition, boundary layer transition was achieved.

In Fig. 3.3 an instantaneous snapshot of the flow around the straight edge NACA 0018 wing is shown. From this figure it can be seen that the flow accelerates on the first 20% of the wing after which it encounters the zig-zag strip and a turbulent boundary layer appears along the back of the wing. Behind the wing a big wake can be observed in the instantaneous snapshot, which is due to the relative low Reynolds number used in the simulation, or by over-tripping the boundary layer. In Fig. 3.4 the time-averaged velocity magnitude for the same case is presented. From this image it can be seen that the flow is symmetric which is as expected for the symmetric NACA 0018 airfoil under zero angle of attack.

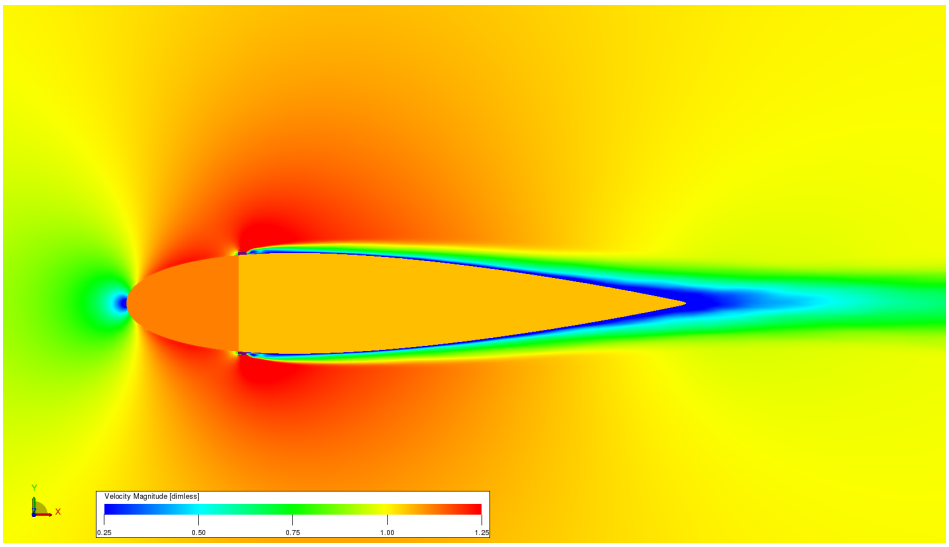

Figure 3.4: Time-averaged velocity magnitude mid span of the NACA 0018 wing.

A turbulent boundary layer is typically characterised by the vortical structures within. The generation of turbulence is visualised in Fig. 3.5 by means of iso-contours of λ_2, which is defined as the second invariant of the velocity tensor. A close up of the turbulence generation around the zig-zag strip on the upper surface can also be seen in the figure. Just downstream of the zig-zag strip, hairpin-like structures can be observed which break down into smaller scale vortical structures, indicating the development of a turbulent boundary layer.

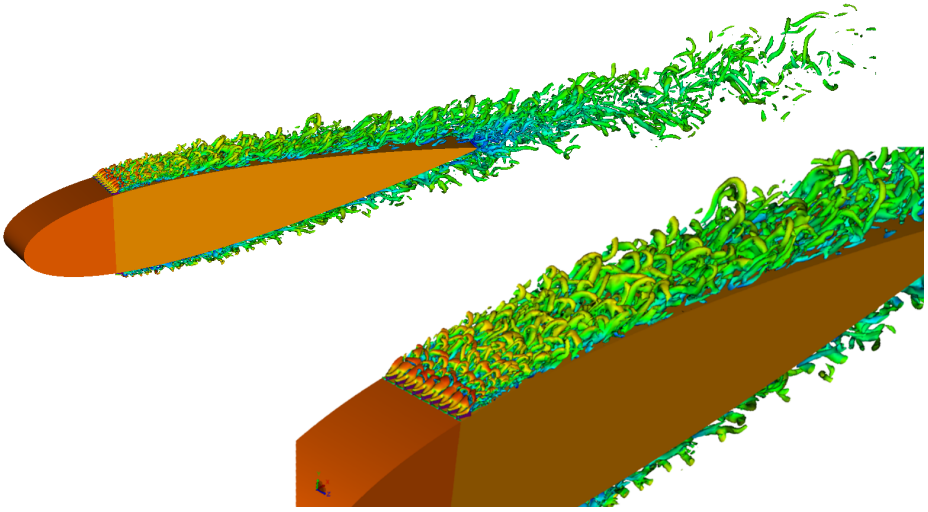

Figure 3.5: Generation of turbulence by the zig-zag strips visualised by means of λ_2 iso-contours for the fine mesh, coloured by velocity magnitude.

In order to characterise the boundary layer thickness of the trailing edge of the wing, the boundary layer edge has been identified using the spanwise vorticity. The widely used defini-

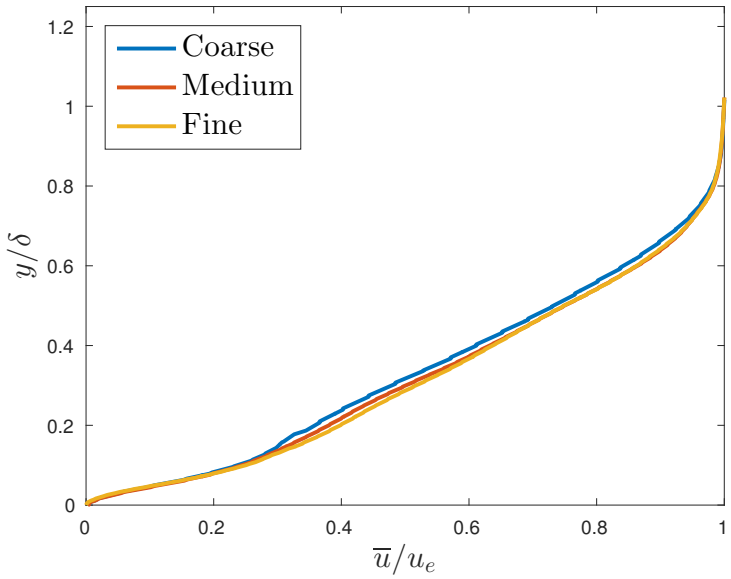

Figure 3.6: Time-averaged boundary layer profile at the trailing edge for the three different mesh cases.

tion of the boundary layer thickness, δ_{99}, is the position where the local velocity equals 99% of the free stream velocity. However, this method is less applicable due to the fact that a pressure gradient is involved in this case, and the freestream velocity is not reached outside the boundary layer. Therefore, the time-average spanwise vorticity is a good indication of the boundary layer thickness. The boundary layer thickness is determined by the position where the variation in absolute spanwise vorticity is zero.

The resulting boundary layer thickness, i.e. δ_100, at mid span, λ, for the three different mesh setups are 0.0195 m, 0.0198 m and 0.0197 m, respectively. The boundary layer size are used to normalise the boundary layer parameters for each mesh setup separately.

The difference in the boundary layer profile at the trailing edge (at 100% chord) is shown in Fig. 3.6. The velocity profiles are acquired by averaging around 4000 samples over 0.075 second (15 flow passes). The lower 10% of the boundary layer locates the inner refinement volume. Although the level of refinement is different in this area for the different meshes the resulting profile is identical. A difference in velocity is seen in the intermediate region of the boundary layer. For $0.3 \leq y/\delta \leq 0.9$ the coarse mesh deviates the furthest from the fine mesh solution. The differences between the medium and fine mesh are relatively small and for a limited region of $0.3 \leq y/\delta \leq 0.6$.

Apart from the boundary layer thickness several characteristic parameters can be retrieved from the boundary layer profiles. The displacement thickness δ^* can be calculated by integrating the velocity deficit over the boundary layer height using (Pope (2000)):

$$\delta^* = \int_0^\delta \left(1 - \frac{\bar{u}(y)}{u_e}\right) dy. \tag{3.1}$$

A similar formula exists for the momentum thickness (Pope (2000)):

$$\theta = \int_0^{\delta} \frac{\bar{u}(y)}{u_e}\left(1 - \frac{\bar{u}(y)}{u_e}\right) dy. \tag{3.2}$$

In these equations $\bar{u}$ indicates the time-averaged velocity in the x-direction, and u_e the velocity at the boundary layer edge.

When dividing these two parameters the kinematic shape factor, H, of the boundary layer is retrieved:

$$H = \frac{\delta^*}{\theta}. \tag{3.3}$$

For a flat plate boundary layer a fully developed turbulent boundary layer exists for $H = 1.3 - 1.5$. However, due to a pressure gradient this number can increase (Pope (2000)). As the NACA 0018 has a significant adverse pressure gradient, even at zero angle of attack, the obtained shape factors for the different mesh cases deviate from $1.3 - 1.5$.

In Tab. 3.4 the boundary layer parameters discussed above are presented for the different mesh setups. As can be seen from the table the boundary layer thickness does not deviate much between the different mesh setups, especially for the medium and fine mesh. A similar pattern can be seen for the displacement thickness δ^*, momentum thickness θ and edge velocity u_e. This might be due to the small y^+ values used in the three setups. There is however a small difference noticeable in the shape factor. Yet, the relatively difference is rather small with around 3.5% between the coarse and fine mesh. The resulting shape factor for the three different mesh cases all deviate significantly from the flat plate value of $1.3 - 1.5$. To see whether these values are reasonable XFOIL is used to calculate the shape factor of a two-dimensional NACA 0018 airfoil under the same flow conditions of $\mathcal{R}e = 40,000$ and $M = 0.116$. Tripping of the boundary layer was done on both the suction and pressure side at 20% chord, similar to the simulations. XFOIL is an open-source program developed by Drela (1989) for the design and analysis of subsonic isolated (two-dimensional) airfoils. The resulting kinematic shape factor obtained with XFOIL at the trailing edge of the airfoil was 2.59, which is around 13% higher than the values found from the simulations. As XFOIL is a panel method using several (empirical) models to acquire boundary layer characteristics the results are not an exact representation of real life. The value by XFOIL, however, indicates that the shape factor found from the simulations is not too high.

Mesh case	δ $[m]$	δ^* $[m]$	θ $[m]$	H $[-]$	U_e $[m/s]$
Coarse	0.0195	0.0060	0.0026	2.3278	39.0127
Medium	0.0201	0.0059	0.0026	2.2852	38.9221
Fine	0.0201	0.0059	0.0026	2.2479	38.9223

Table 3.4: Boundary layer parameters for the different mesh setups for the straight trailing edge wing.

In Fig. 3.7 the Reynolds stresses at the position of the trailing edge are plotted for the different mesh cases. As can be seen from the figure, large variations exist between the different mesh setups. Overall the trends seem non-converged, possibly due to a lack in sample size, which

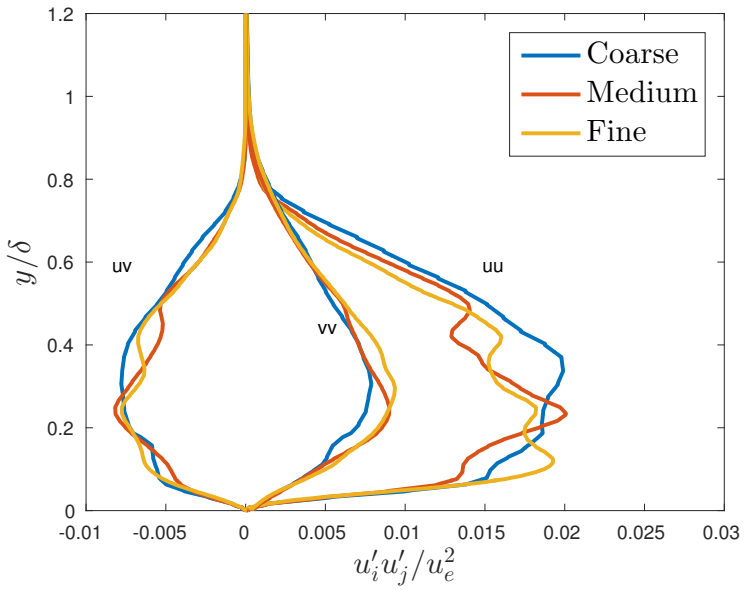

Figure 3.7: Time-averaged Reynolds stresses at the trailing edge for the three different mesh cases.

was of 15 flow passes. For the wall normal component, the medium and fine grid solution show little deviation. Also for the streamwise and shear stress components the curves for the medium and fine grid are closer compared to the coarse mesh solution.

Apart from the boundary layer characteristics, the pressure distribution around the airfoil can be retrieved from XFOIL. The time averaged pressure coefficient, C_p, along the mid span on the upper side of the wing surface has been extracted from the three different simulations and are presented in Fig. 3.8 together with the reference curve of XFOIL. As the airfoil and flow conditions are symmetric the curves corresponding to the lower side of the airfoil are almost identical to the coefficients on the upper side and are therefore not plotted for clarity. The pressure curves closely resemble the solution found by XFOIL away from the trip location ($x/c = 0.2$). Just upstream of the zig-zag strip location, the pressure decreases rapidly after which it increases beyond the value found using XFOIL. A similar trend has been seen by de Jong (2012) near the boundary layer tripping devices. The time-averaged pressure coefficients are almost identical between the different mesh setups. The frictionless wall condition might influence the behaviour upstream of the trips, causing the pressure curves to deviate from the XFOIL result.

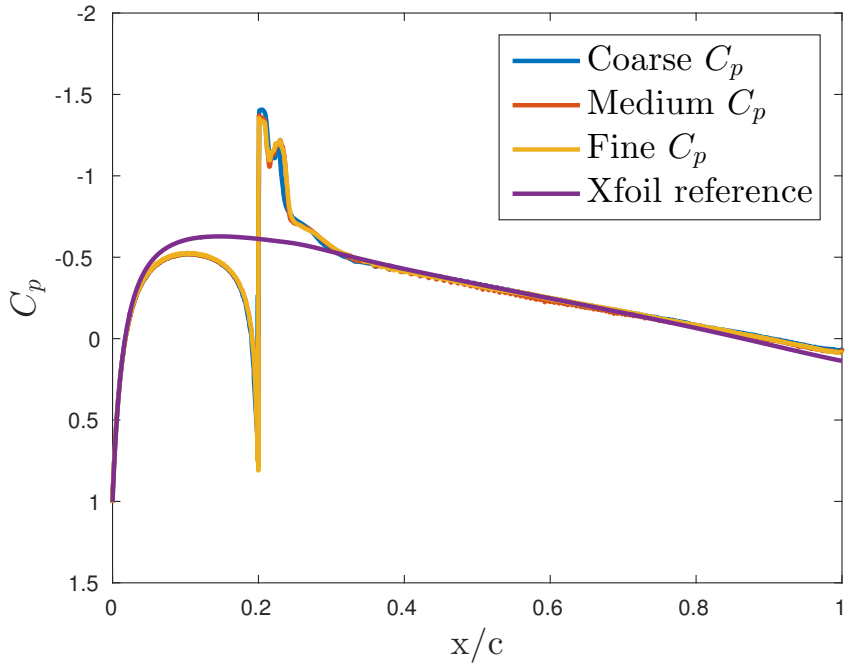

Figure 3.8: Time-averaged pressure coefficient along mid span on the upper side of the wing for the different mesh cases including solution of XFOIL.

The results for the flow field show that the different mesh sizes do have little deviation between them. The boundary layer thickness, pressure distribution and shape factors are all within 5%. For the boundary layer profile one might say that the medium and fine mesh seem almost identical while the coarse mesh deviates. In the next section the far field acoustics are presented to distinguish any differences in the noise spectrum.

3.2.2 Acoustic emissions

Now that the resulting flow field has been examined and only little deviation was found between the different mesh setups, the results for the acoustic far field spectrum are considered.

At the location positioned directly above mid span of the wing trailing edge (90°) the power spectrum is extracted using the three different methods described in Chapter 2. The pressure information captured by the direct probes in the computational domain is converted to a sound pressure level (SPL). The aeroacoustic SPL, Φ_{aa}, is found using the following formula:

$$\Phi_{aa} = 10 \log_{10} \left(\frac{p'}{p_{ref}} \right)^2, \tag{3.4}$$

where p' is the pressure fluctuation relative to the pressure at rest and $p_{ref} = 2 \times 10^{-5}\ Pa$ is the reference sound pressure. The output of the Curle and FW-H analogy is also plotted

in means of the SPL. In order to compare the direct probes with the acoustic analogies the sound pressure level is scaled to a reference case with a Mach number of M = 1, an observer radius of r = 1 m and a span of b = 1 m by means of:

$$\Phi_{scaled} = +10 \log_{10} \left(\frac{r^2}{bM^5} \right). \tag{3.5}$$

In addition to the previous scaling, another correction has to be applied to the sound spectra found by the direct probes. This correction is due to the cyclic boundary conditions and limited span, which results in the acoustic pressure field in the numerical solution to contain contributions from mirrored coherent image sources of the airfoil arriving through the cyclic domain boundaries to the microphone location. Oberai et al. (2002) came up with a three-dimensional, frequency dependent correction for low Mach number flows, which can be expressed in dB form as:

$$\Phi_{cyclic} = +10 \log_{10} \left(\frac{fb^2}{a_0 r} \right). \tag{3.6}$$

Using these corrections the resulting sound pressure level directly above the wing has been calculated. In Fig. 3.9 the SPL for the direct probes for the Strouhal spectrum is presented for the three different mesh setups. The Strouhal (St) number is the dimensionless frequency and is defined as:

$$St = \frac{fc}{u_\infty}. \tag{3.7}$$

From this figure it can be seen that the cut-off frequency is identical for different meshes, which is represented by the plateau at high frequencies. This similarity is expected as the voxel size at the probe location is not changed between the different mesh setups.

Due to the fact that the sound pressure level in the region near the noise plateaus is significantly lower than the SPLs at the lower end of the spectrum these a close-up of the remaining is shown in Fig. 3.10 .

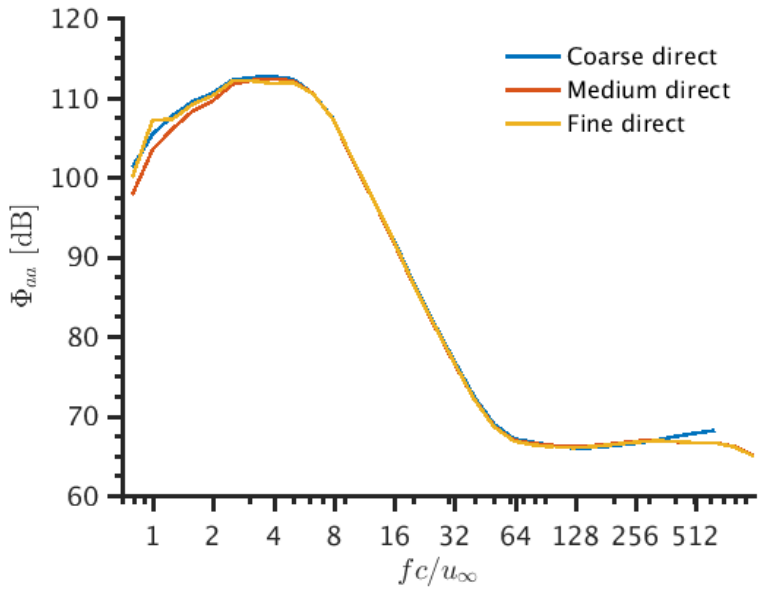

Figure 3.9: Observer and span normalised far field sound pressure level of the direct probes for different mesh resolutions.

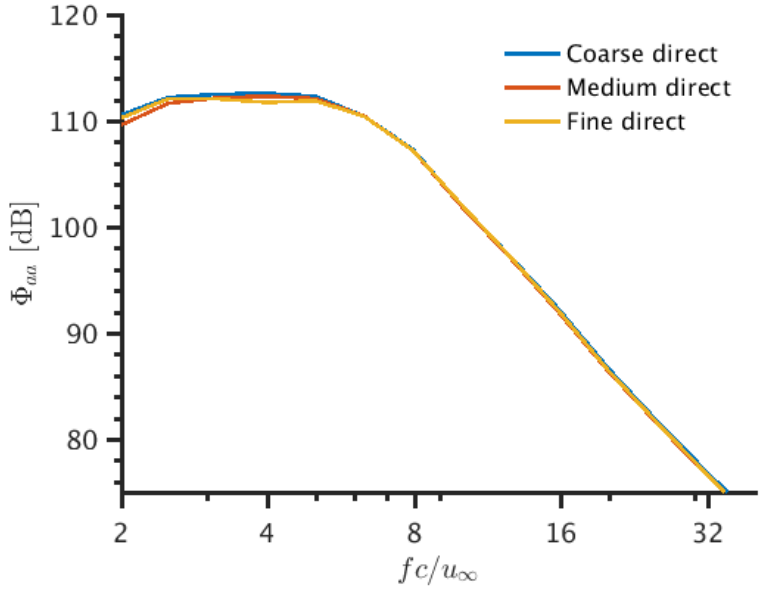

Figure 3.10: Close up of observer and span normalised far field sound pressure level of the direct probes for different mesh resolutions.

When looking at the spectrum for Strouhal numbers between 2 and 40 one can see that the far field sound pressure level found by the different simulations does not seem to vary much. The overall trend is similar for the different mesh cases. Higher sound pressure levels at the lower end of the spectrum with a decay at larger Strouhal numbers. The power spectra show a broadband noise without any sharp peaks indicating no clear vortex shedding at the trailing edge. There is no significant difference noticeable in the sound pressure level found using the direct probes.

When using the analogy of Curle the sound spectra differ slightly as can be seen in Fig. 3.11. This figure illustrates the different cut-off frequencies of the different meshes when using the solid surface pressure fluctuations as input instead of the direct pressure probes. The voxel size near the solid wing is identical for the medium and fine mesh but is of 1 order of refinement smaller, making the deviation with the coarse curve apparent at high frequencies.

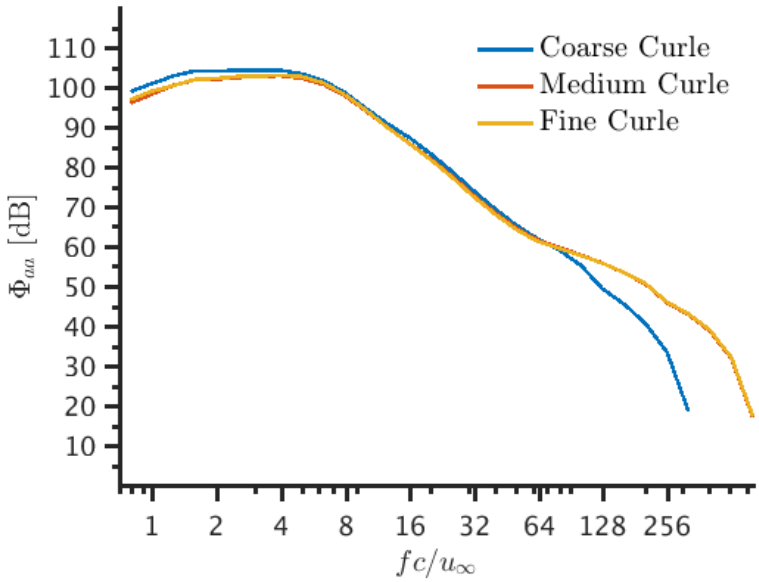

Figure 3.11: Observer and span normalised far field sound pressure level of the Curle analogy for different mesh resolutions

When zooming in on the most dominant part of the spectrum presented in Fig. 3.12 a noticeable difference is visualised between the coarse and the other two meshes at low frequency. Along this entire range of frequencies the coarse simulation results in an over-prediction of the sound pressure level. This over-prediction of around 1-2 dB is significant as a doubling of acoustic power equals a 3 dB increase.

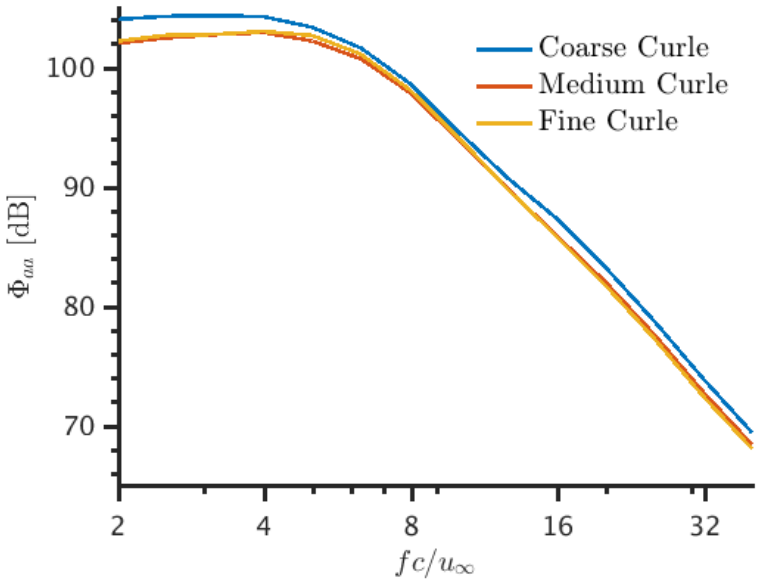

Figure 3.12: Close up of observer and span normalised far field sound pressure level of the Curle analogy for different mesh resolutions

In Fig. 3.13 the results of three different methods for capturing the far field acoustic spectrum are presented. The difference between the Curle and FW-H analogy in the Strouhal number range of $2 < St < 40$ is insignificant. A small deviation exists at the higher end of the spectrum. This might be caused by the quadrupole sources surrounding the trailing edge that produce high frequency noise. As these sources are located within the funnel surrounding the wing the sources are captured by the FW-H analogy but not by the Curle analogy, which only uses wing surface information.

The difference between the results found by the direct probes and the other two analogies is remarkably large. This difference in sound pressure level was not found in the LES simulations by van der Velden et al. (2016). A possible explanation for this is that the direct probes are located in a refinement volume of scale 4, where the desired viscosity could not be achieved by the DNS. In the simulations by van der Velden et al. (2016) the desired viscosity was achieved in the entire domain. The change in viscosity seems to result in an over-prediction of the sound power level by the direct probes. The change in viscosity may change the propagation characteristics leading to this over-prediction. Therefore the direct probes in these DNS simulations seem less effective in predicting the power spectra.

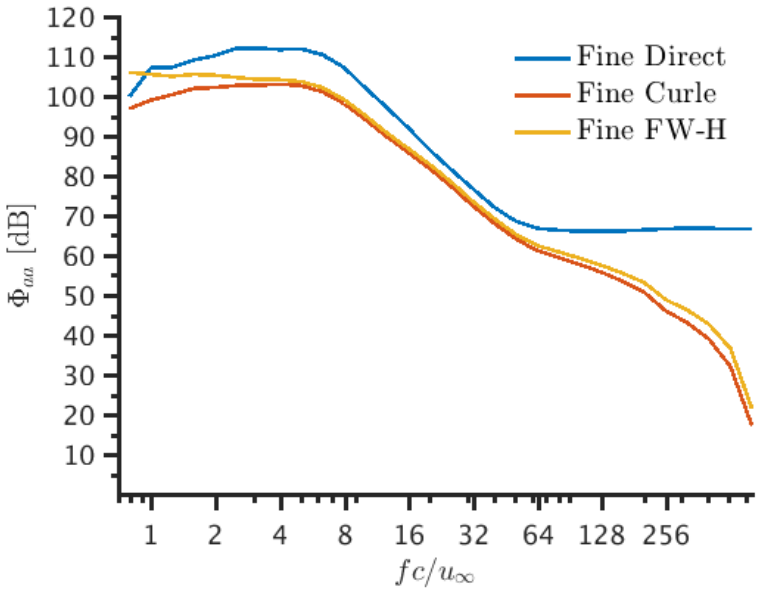

Figure 3.13: Observer and span normalised far field sound pressure level for the different acoustic methods for the fine mesh.

To compare the total noise between the different cases the overall averaged sound pressure level (OASPL) is defined as:

$$OASPL = 10log_{10}\left[\sum(10^{SPL_i/10})\right], \tag{3.8}$$

where SPL_i is the i-th sound pressure level per $\frac{1}{3}$-octave frequency band for the range of $St = 2 - 32$.

The total noise power for the entire frequency regime (i.e. $St = 2 - 32$) for the different mesh setups and the corresponding acoustic methods are tabulated in Tab. 3.5. As seen before the direct probes result in remarkable higher values for the overall produced sound. When comparing the values for the different meshes one can see that the coarse mesh deviates from the medium and fine mesh for the acoustic analogies. The results of the medium and fine mesh differ around 0.5 dB, compared to around 1 dB for the coarse mesh, suggesting that the medium mesh is accurately capturing the sound emission.

Mesh case	Direct probes	Curle analogy	FW-H analogy
Coarse	130.0460	103.9459	105.2061
Medium	129.8238	102.4998	103.5982
Fine	129.7304	103.1117	104.0993

Table 3.5: Overall sound pressure level in dB for the different meshes and acoustic methods.

Apart from the position directly above the trailing edge the acoustic spectrum around the entire airfoil can be computed, to acquire a directivity pattern for the different mesh setups. For this an array of 360 microphones in a cylindrical pattern are placed around the trailing edge at 10 chords radial distance to record the acoustic pressure fluctuations derived by the

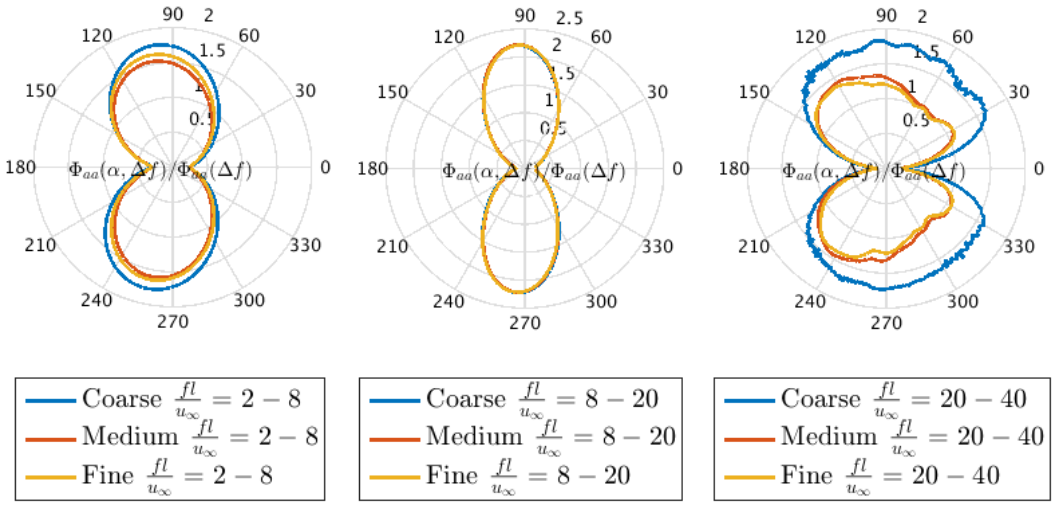

Figure 3.14: Averaged directivity pattern for three frequency regimes for different mesh setups.

Curle analogy method. The resulting directivity plots for different Strouhal number regimes are plotted in Fig. 3.14. The pressure levels are normalised by the average of the fine pressure values on that certain frequency regime.

At low Strouhal numbers a compact dipole source arises from the trailing edge which is tilted slightly forward. For high Strouhal numbers the directivity plot shows that the noise is not located in a particular direction but scattered in multiple directions. This is typical non-compact behaviour, where not only source radiation but also source-body interactions take place. For Strouhal numbers in the intermediate regime the directivity is not as expected. When increasing the frequency from $St = 2-8$ to $St = 8-20$ the expected behaviour is that the dipoles tilt more forward as seen in the simulations by van der Velden et al. (2016). From the figures you can see that there is a slight tilt forward, yet this is insignificant compared to the low frequency result. The reason for this unexpected directivity results remains unclear, and would need further investigations.

3.3 Closing statement

Three different mesh sizes have been used to simulate the flow field around and far field acoustics of a straight trailing edge NACA 0018 wing. The results for both the flow field and the acoustics converged for increasing grid resolution. Little difference was found between the intermediate and finest mesh setup, where the coarsest mesh deviates slightly from the others. Due to the already high accuracy of the medium grid, the medium mesh setup will be used in the simulation of the serrated trailing edge airfoil. The directivity plots for the intermediate frequency range deviate from the expected results. The difference between the results retrieved by the Curle and Ffowcs Williams & Hawkings analogies is limited, where the direct probe sound pressure level deviates due to viscosity scaling in the regions outside the boundary layer.

Chapter 4

Trailing edge add-ons

4.1 Sawtooth serrations

As explained in the introduction the serration type of interest are the sawtooth type, as the sawtooth trailing edge will perform better than the sinusoidal edge according to Howe (1991b). The sawtooth trailing edge has the potential to decrease the noise produced by the straight edge wing from the previous chapter significantly.

4.1.1 Setup

The setup exists of the same NACA 0018 wing model as in the previous chapter with the addition of a serrated edge attached to the trailing edge. The dimensions of the serrations is equal to the ones used in the numerical setup of van der Velden et al. (2016) and the experimental campaign of Arce Léon et al. (2016a,b). Due to the limited span for the DNS simulations in this thesis a single serration is the maximum that can be achieved. The serration has a length of 0.04 m ($2h = 0.2c$) and a width of 0.02 m ($\lambda = 0.1c$), resulting in a length-to-width ratio of $\lambda/h = 1$. This ratio meets the criteria by Howe (1991b), who suggests a ratio of $\lambda/h < 4$. The serrations are of a flat-plate type and are attached to the trailing edge with zero degrees inclination. The thickness of the serration is constant to 1 mm ($t = 0.005c$) in both length and span. In Fig. 4.1 the serrated NACA 0018 model with is shown. The mesh setup is similar as the medium mesh setup for the unserrated case. The finest refinement scale of VR 7 is used in the region with an offset of 20 mm around the wing surface, which includes the region surrounding the serration.

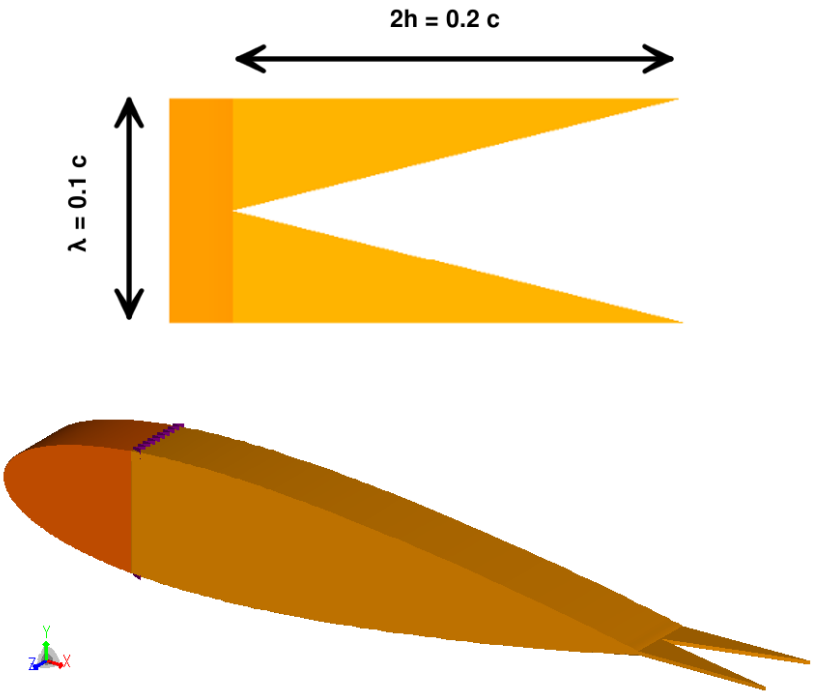

Figure 4.1: Isometric view of the serrated NACA 0018 wing, with a close-up topview of the serrations.

4.1.2 Results

The results for the serrated trailing edge simulations are presented in this section. As in the previous chapter, this section is split into two parts. First the results for the flow field are presented after which the acoustic emission results are shown and discussed.

Flow Field

To compare the flow characteristics between the clean and serrated wing, three different points along the serration edge are used. Values at the tip, halfway and at the root of the serrated edge are compared with the trailing edge values of the clean wing.

The boundary layer profile is plotted in Fig. 4.2 for the serrated and clean wing setup. From this figure one can see that the velocity profile at the root of the serration is almost identical to the unserrated wing profile at the same location. This might suggest that the serrations do not affect the boundary layer upstream of the trailing edge. Further downstream the flow is accelerated in the boundary layer for $y/\delta \leq 0.8$. The boundary layer thickness at the different locations is determined as before, using the spanwise variation of vorticity.

The boundary layer characteristics at the different locations on the serrations are presented in Tab. 4.1 together with the straight trailing edge values. All boundary layer parameter values reduce in size from the root towards the tip of the serration. Remarkable is that the

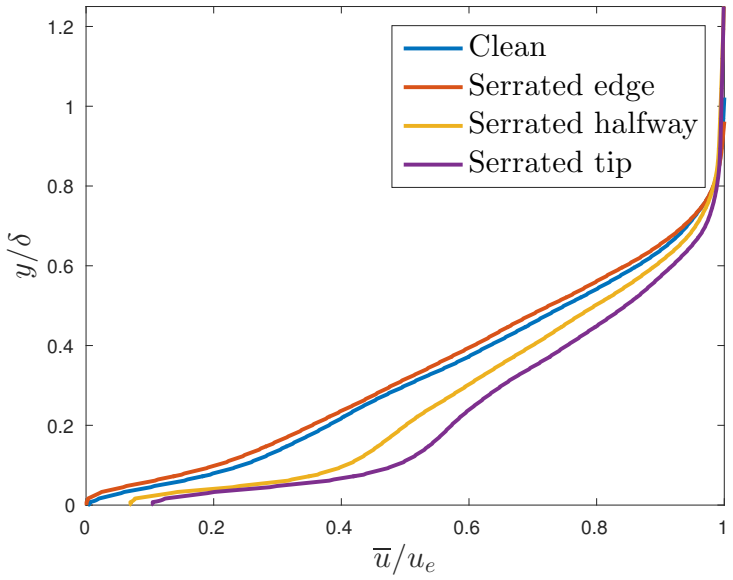

Figure 4.2: Boundary layer profile at different locations on the serrations together with the straight trailing edge result.

values at the root of the serrated edge are higher than for the straight trailing edge. This contradicts the assumption made by Howe (1991a,b) that the turbulence is frozen and thus does not change by introduction of the serrations. The accelerated flow in the boundary layer downstream of the trailing edge stretches and elongates the local turbulent structures.

Location	δ $[m]$	δ^* $[m]$	θ $[m]$	H $[-]$	U_e $[m/s]$
Root	0.0223	0.0063	0.0026	2.4107	39.1384
Halfway	0.0204	0.0047	0.0026	1.8505	38.7277
Tip	0.0195	0.0040	0.0024	1.6954	38.7401
Straight edge	0.0201	0.0059	0.0026	2.2852	38.9221

Table 4.1: Boundary layer parameters at different positions on the serration together with the straight edge.

In Fig. 4.3 the Reynolds stresses at the different locations on the serration are plotted. From this figure one can see that the general shape of the curves does not differ at the different locations. However, the maximum value of the fluctuations halfway and at the tip of the serrations is decreased compared to the clean case, especially for the streamwise component. As turbulent fluctuations are linked to produce sound it suggests that the sound production downstream of the root is smaller.

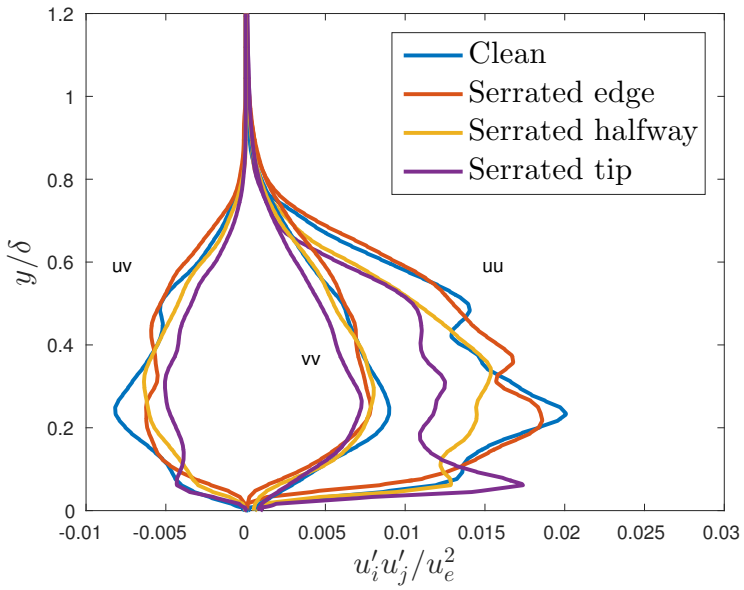

Figure 4.3: Time-averaged Reynolds stresses at different locations on the serration together with the straight trailing edge result. cases

In order to see the detailed flow pattern near the serrations the time-averaged streamlines at the location of the serration are shown in Fig. 4.4. From this picture one can see that the streamlines (coloured by non-dimensional height) are drawn downward into the gap between the serrations at the serration edges. This might be caused by a Coandă effect where the flow has a tendency to stay attached to the body surface even when it curves away. Another explanation is that the additional volume in the gap is occupied by the fluid due to conservation laws. A small low pressure region forms behind this 1 mm edge which deviate the flow towards this region. In the top view presented in Fig. 4.5 one can see that the flow is also deflected in spanwise direction. The local angle between the flow direction and serration edge increases at the edge location, which is unfavourable for noise mitigation, according to Howe (1991b). Near the root of the serration the flow direction seems more unfavourable than near the tips. This spanwise deflection contradicts the assumption made by Howe (1991b) that the local flow angle is unchanged due to the serrations. This might cause the overprediction of noise reduction by Howe compared to other studies. The prediction of Howe might be accurate for the flow near the serration tips but not at the root. In the wake of the serration a wavy pattern of streamlines at higher and lower vertical positions can be observed.

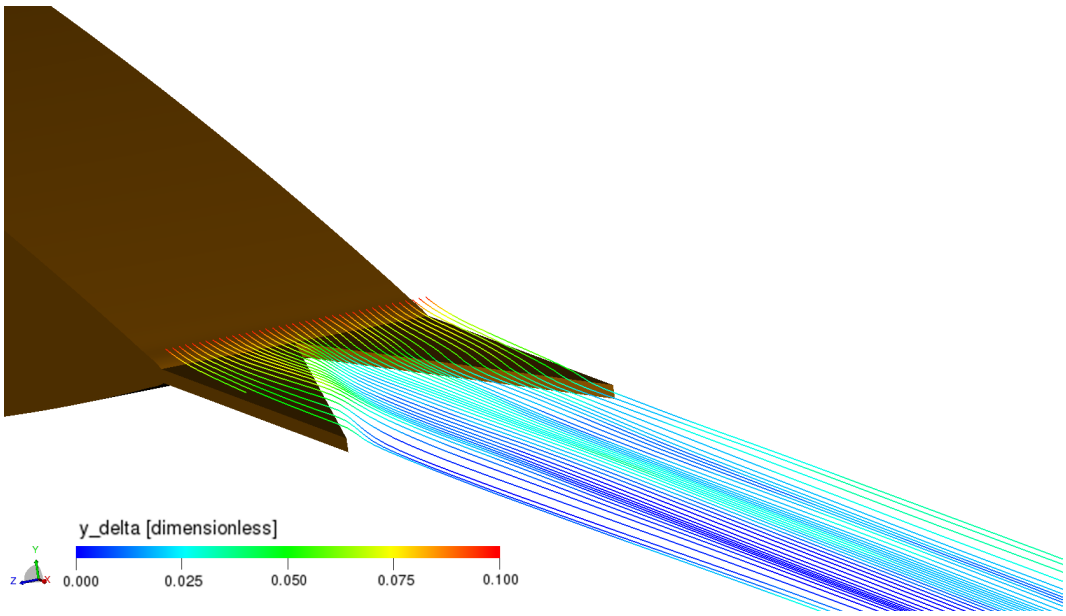

Figure 4.4: Isometric view of streamlines on around the serrations at the trailing edge. Streamlines coloured by height non-dimensionaled by boundary layer thickness at the trailing edge.

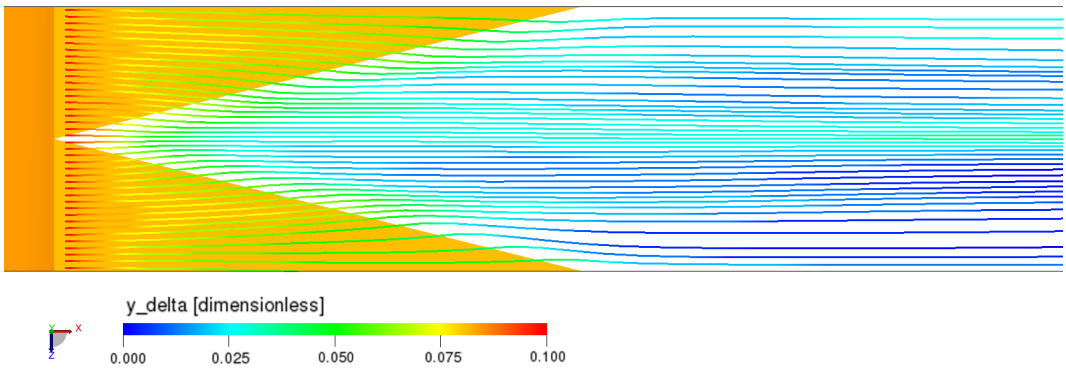

Figure 4.5: Top view of streamlines on around the serrations at the trailing edge. Streamlines coloured by height non-dimensionaled by boundary layer thickness at the trailing edge.

As the turbulent fluctuations in the wake of the wing are also expected to produce sound the difference in the wake of the straight and serrated trailing edge are also compared. The time-averaged vorticity magnitude at cross-sectional planes $0.1c$, $0.2c$, and $0.3c$ behind the trailing edge of the straight and serrated trailing edge are shown in Fig. 4.6. From this figure one can see that the vorticity is similar in magnitude at $0.1c$ behind the trailing edge, i.e. halfway the serrations, for the serrated and straight trailing edge. Further downstream the vorticity magnitude is smaller for the serrated wing, and it also appears to be more smooth. This might suggest that the turbulent fluctuations in the wake of the serrations are reduced and therefore the sound produced by the quadrupole sources at these locations might be reduced.

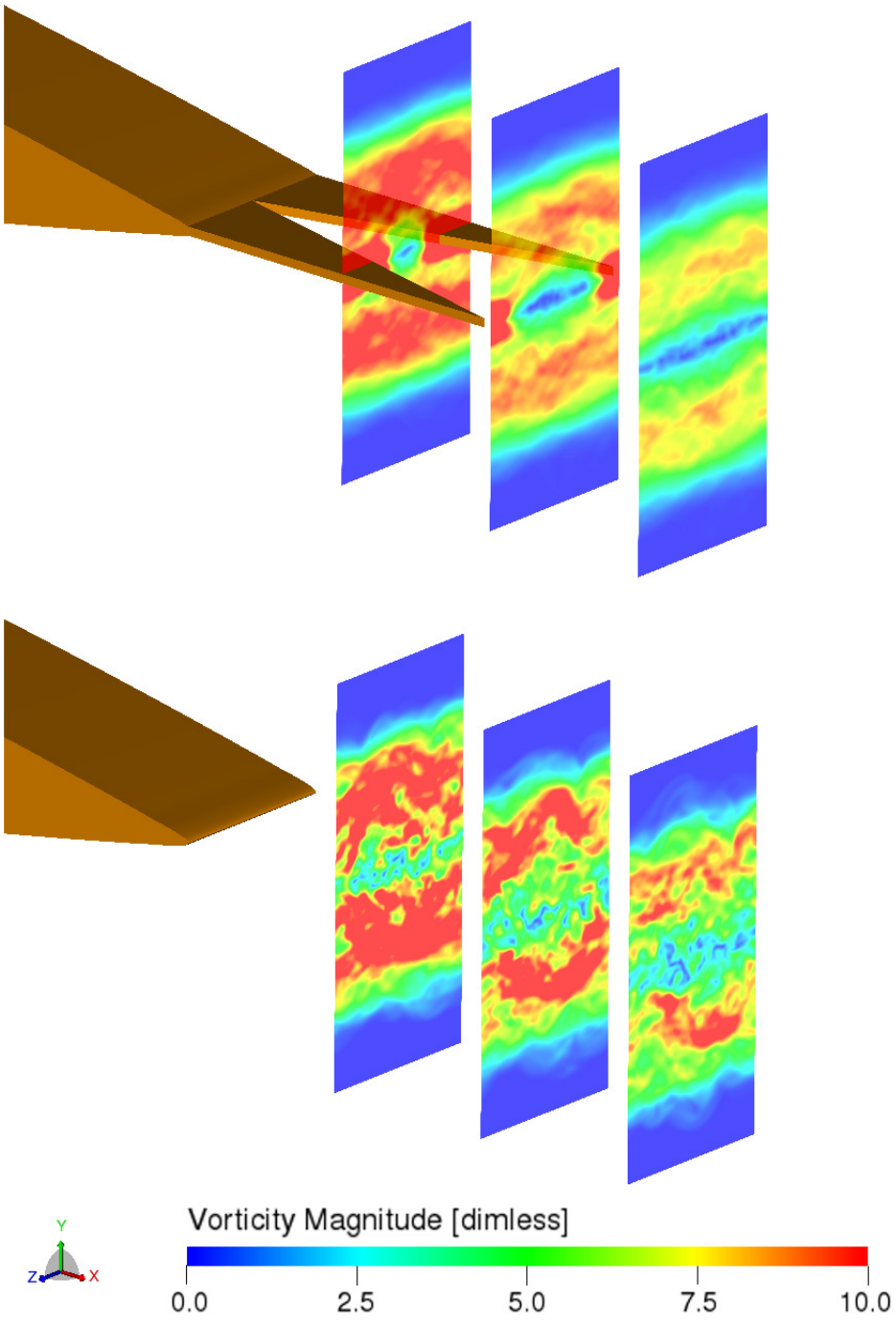

Figure 4.6: Time-averaged vorticity magnitude behind the trailing edge for the serrated (top) and straight (bottom) trailing edge. XZ-Planes are $0.1c$, $0.2c$, and $0.3c$ behind the trailing edge respectively.

Acoustics

As the flow field does not follow the patterns assumed by Howe (1991b) the acoustic noise generation is also expected to deviate from his theory. The prediction by Howe for the sawtooth trailing edge is a noise reduction of $10log_{10}[1 + (4h/\lambda)^2]$ dB, which results in a reduction of around 12.3 dB. In Fig. 4.7 the sound pressure levels from the Curle analogy for the clean and serrated wing are shown. From this figure one can see that the overall shape of the curves is similar. However, the serrated wing produces significantly less noise compared to the clean wing for $St < 8$. For high frequencies the sound produced by the serrated wing is similar to slightly higher. A similar pattern can be seen when the sound pressure level reduction is plotted for the different analogies and the direct probes, see Fig. 4.8. From this figure one can see that the predicted reduction is similar for the Curle and FW-H analogy, while the direct probes show lower reduction for low frequencies. When looking at the results for the Curle and FW-H analogies one can observe that the maximum reduction occurs at around $St = 3$ or a frequency of 600 Hz. The maximum reduction is around 3 dB, which corresponds to a significant reduction of approximately 50% in power. However, this reduction is far lower than the predicted value of 12.3 dB by Howe (1991b).

For high frequencies a sound increase of approximately 0.5 dB is acquired for the three different methods. From this figure it seems that the serrations shift the noise output from low to the high frequency regime, which has been observed before by e.g. Oerlemans et al. (2007).

The result for the sound reduction of the experimental study on the same wing and serrations of Arce Léon et al. (2016b) show a maximum reduction of around 6 dB at a frequency of 1450 Hz ($St \approx 8.3$) for a free stream velocity of 35 m/s and a Reynolds number of around 4.5×10^5. As the conditions are different a direct comparison in frequency spectrum is unreliable. Not only is there a difference in free stream velocity, but the difference in Reynolds number results in a thicker boundary layer at the trailing edge, which seems to be an important parameter for sound emission according to for example Oerlemans (2011); Howe (1991b).

Defining a Strouhal number based on boundary layer thickness at the straight trailing edge:

$$St_\delta = \frac{f\delta}{u_\infty}, \tag{4.1}$$

and the following based on boundary layer displacement thickness at the straight trailing edge:

$$St_{\delta^*} = \frac{f\delta^*}{u_\infty}. \tag{4.2}$$

The resulting frequency scaling is shown on the top of Fig. 4.8. When applying the same scaling to frequency at maximum reduction found by Arce Léon et al. (2016b); van der Velden et al. (2016), the maximum reduction of Arce Léon et al. (2016b) is located at $St_\delta = 0.389$ and $St_{\delta^*} = 0.087$, and at $St_\delta = 0.388$ and $St_{\delta^*} = 0.084$ for van der Velden et al. (2016). When looking at the graph in Fig. 4.8 one can see that maximum reduction occurs at around $St_\delta = 0.3$ and $St_{\delta^*} = 0.09$. The frequency at maximum reduction is remarkable close when scaled with the boundary layer displacement thickness. This suggests that the maximum effectiveness of the trailing edge serration can be found at $St_{\delta^*} \approx 0.09$. Also the frequency

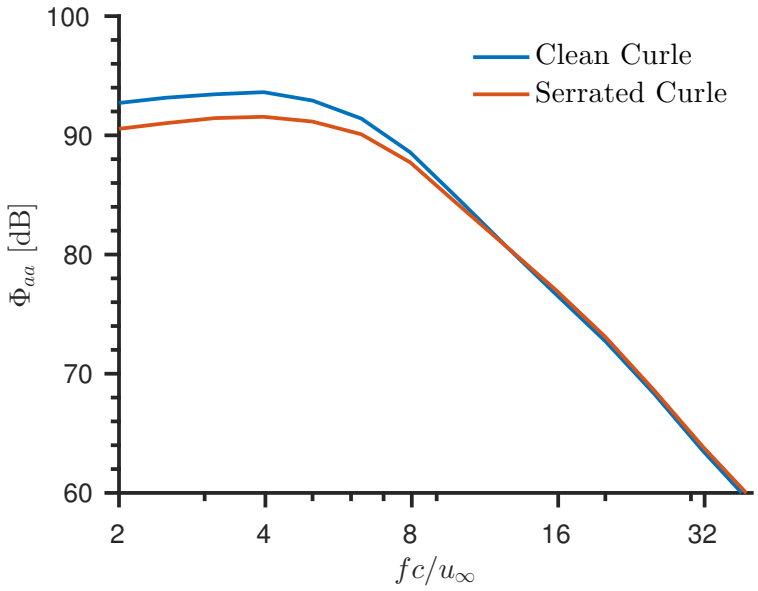

Figure 4.7: Observer and span normalised far field sound pressure level from the Curle analogy for the clean and serrated wing.

at which serrations seem ineffective in reducing noise is similar when expressed in St_{δ^*}. For $St_{\delta^*} > 0.23$ a noise increase is seen in this study as well as in Arce Léon et al. (2016b); van der Velden et al. (2016). This suggests that the trailing edge serration is effective up to $St_{\delta^*} \approx 0.23$.

The influence of the trailing edge serrations on the entire frequency regime (i.e. $St = 2 - 32$) is visible in Tab. 4.2, where the OASPL is tabulated for the straight and serrated trailing edge together with the predicted reduction by Howe (1991b). As seen before the OASPL obtained using direct probes is much higher than for the acoustic analogies; also the overall reduction is significantly lower at around 0.5 dB. The reduction obtained using the acoustic analogies does not deviate much with an overall reduction of around 2 dB. The overall reductions for all methods are far lower than the prediction by Howe, suggesting his prediction is too optimistic.

	Direct probes	Curle's analogy	FW-H analogy	Howe (1991b)
Serrated edge	130.0291	102.2284	103.8099	
Straight edge	130.4825	104.1536	105.6209	
Overall reduction	0.4534	1.9252	1.811	12.3

Table 4.2: Overall averaged sound pressure level in dB for the serrated and straight trailing edge wing together with the predicted reduction by Howe (1991b).

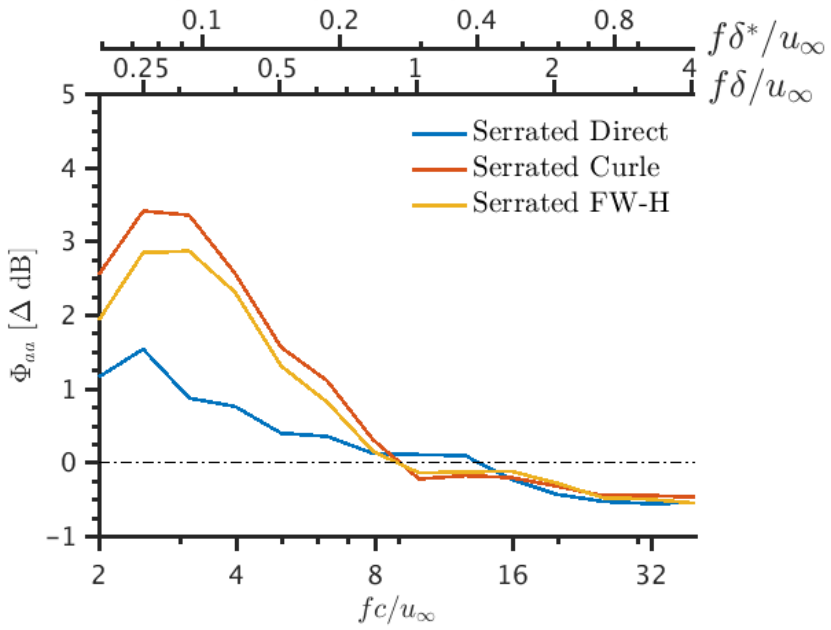

Figure 4.8: Sound pressure level reduction compared to the clean wing for the different acoustic analogies for different frequency scaling.

In order to see in which direction the serrations reduce the noise emissions the directivity pattern is shown in Fig. 4.9. In this figure the pressure levels are normalised by the average of the unserrated pressure values on that certain regime. As with the sound pressure spectra the difference is dominant for low Strouhal numbers. For $St = 2 - 8$ the pattern of the serrated wing is similar to the unserrated clean case, but the noise is reduced significantly in almost all directions. The reduction is most dominant at upstream angles, i.e. at 110° and 250°. For $St = 8 - 20$ an almost identical plot is observed. For high frequencies ($St = 20 - 40$) the serrated wing produces slightly higher pressure levels for angles between 30° and 150°.

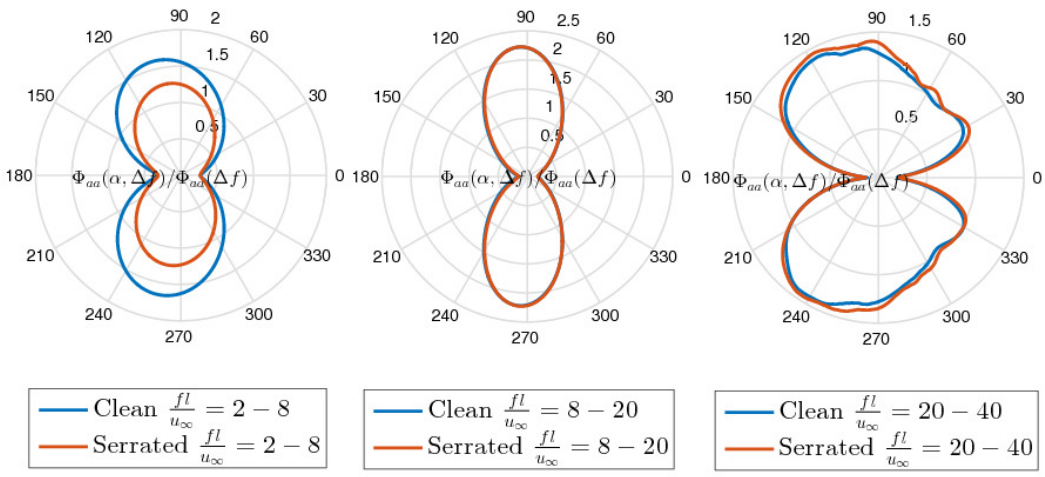

Figure 4.9: Directivity pattern for the clean (straight edge) and serrated trailing edge wing.

As the pressure fluctuations near the surface edges are considered to be related to the sound generation it is useful to compare the surface pressure distributions of the clean and serrated trailing edge. The surface pressure distributions for the three different frequency regimes for the clean and serrated wing are shown in Fig. 4.10. From this figure one can see that for the low frequency regime the pressure fluctuations near the tips of the serrations are significantly lower compared to the straight edge. This can clarify the noise reduction found for the low frequency regime. Near the root of the serration the pressure fluctuations are higher compared to the straight. This is in agreement with the observation made for the flow direction near the serration. At the root the the noise mitigation by the serration seem less effective than at the tips. At higher frequency streaks of higher pressure fluctuations are seen at the serration edges. This confirms the observation that the trailing edge serration shifts the noise from low to higher frequency regime and that the pressure fluctuations are similar between the serrated and straight edge wing at high frequencies.

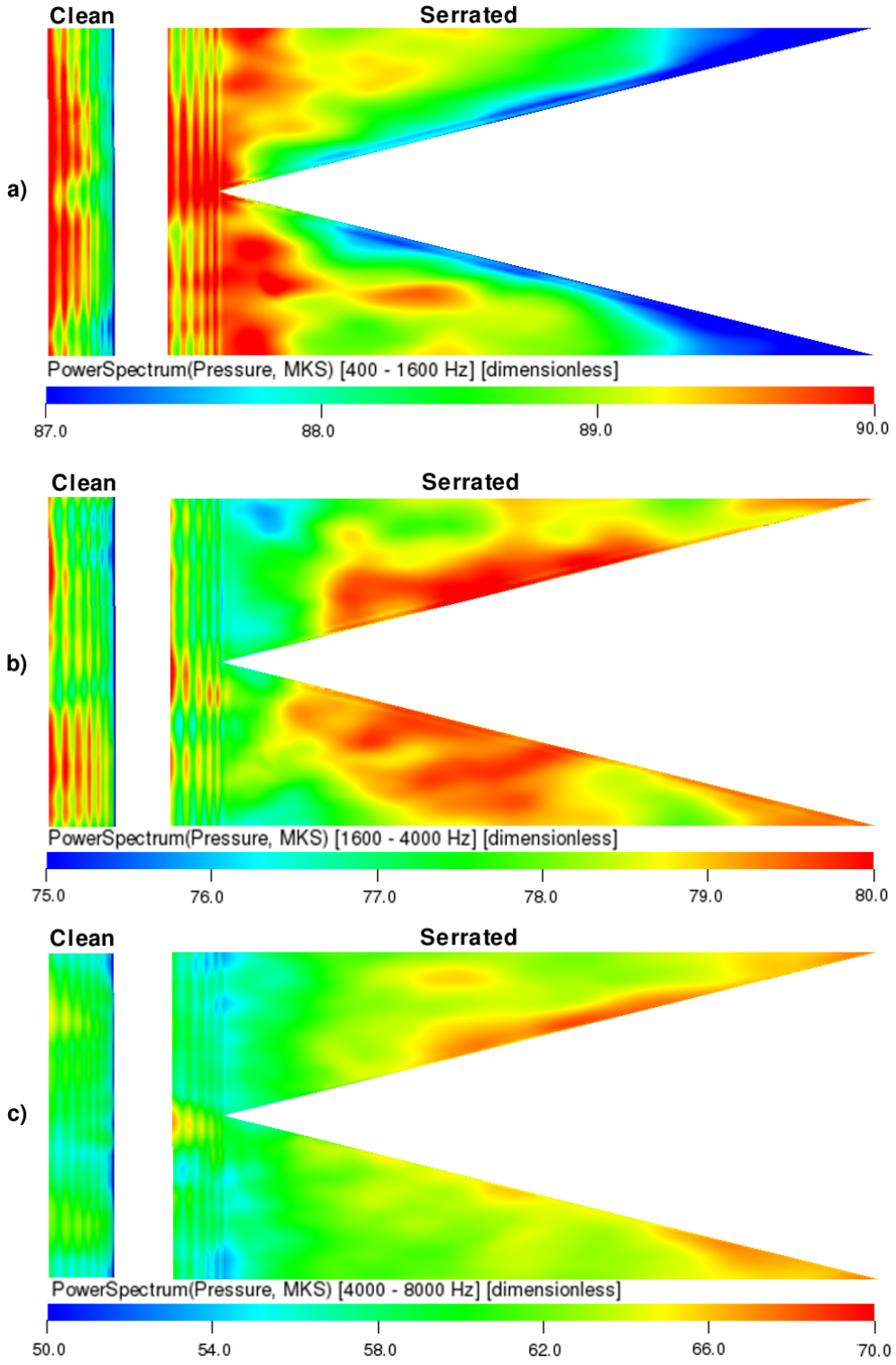

Figure 4.10: Top view of the surface pressure distributions near the trailing edge for clean (left) and serrated (right) for a) $400 - 1600\ Hz$, b) $1600 - 4000\ Hz$, and c) $4000 - 8000\ Hz$.

Chapter 5

Conclusions and Recommendations

5.1 Conclusions

The goal of this research was to reduce trailing edge noise for large wind turbines to potentially increase the widespread use of wind energy, providing substantial benefits for our climate. Trailing edge serrations seem to be a good method for noise source reduction, however optimisation of these add-ons require a deeper understanding of the physics behind trailing edge noise. The research objective of this thesis was to aid the development for improved trailing edge serrations for trailing edge noise reduction by analysing trailing edge noise source generation and propagation to using direct numerical simulations.

In order to know how to accurately simulate the flow and acoustics around a wing with the computational resources available the straight trailing edge simulations were performed first. The analyses was performed on a NACA 0018 wing section of 0.2 m chord of 0.02 m span, at a Reynolds number of 40,000 and a Mach number of 0.116. The simulations were done for three different mesh setups, i.e. coarse, medium, and fine, using three different sound acquiring methods, i.e. direct probes, and the Curle and Ffowcs-Williams & Hawkings acoustic analogies. The results for these simulations converged for increasing mesh size. It was found that the results for the different acoustic analogies were similar for the three different mesh setups. The sound production captured by the direct probes were significantly higher compared to the prediction by the analogies. It was deducted that this might be caused by the change in viscosity for the refinement zone in which the direct probes were located. This change in viscosity resulted in an over-prediction, and so the direct probes do not give an accurate representation of the noise generation. It was concluded that the medium mesh was accurately capturing the flow field, and near and far field acoustics. Therefore the medium mesh was selected as the mesh setup for the serrated wing case.

The simulations performed on the sawtooth trailing edge considered serrations of length 0.04 m and width 0.02 m. From the flow pattern it was concluded that the frozen turbu-

lence assumption by Howe (1991b) is inaccurate. The flow is significantly affected by the introduction of trailing edge serrations, therefore contradicting this theory.

From the flow pattern it was found that the boundary layer is accelerated downstream direction of trailing edge, which results in stretching of the local turbulent structures. Further the Reynolds stresses decrease in the downstream direction on the serration edge, especially for the streamwise component. As turbulent fluctuations are linked to produce sound it suggests that the sound production downstream of the root of the serration is smaller.

From the time-averaged streamlines at the location of the serrations it was shown that the flow is drawn downward into the gap between the serrations at the serration edges, which might be caused by a Coandă effect. Another explanation is that the additional volume in the gap is occupied by the fluid due to conservation laws. Also it was observe that the local angle between the flow direction and serration edge increases at the edge location, which is unfavourable for noise mitigation. Near the root of the serration the flow direction seems more unfavourable than near the tips.

The acoustic results for the serrated trailing edge showed a noise reduction of 3 dB maximum for the acoustic analogies, and an overall reduction of around 2 dB. The predicted noise reduction for the sawtooth trailing edge by Howe is around 12 dB, confirming the over-prediction. A noise increase was observed for frequencies above around 1600 Hz, suggesting serrations shift the noise output from low to higher frequencies.

Comparing the results to recent studies by Arce Léon et al. (2016b); van der Velden et al. (2016) showed that the frequency at which the serrations are most effective can be retrieved by applying frequency scaling. A non-dimensional Strouhal number based on the boundary layer displacement thickness at the straight trailing edge of around 0.09 defines the frequency at which maximum reduction occurs. It is suggested that future research in this field use the same frequency scaling to compare studies at different flow conditions.

The sound propagation of the serrated trailing edge showed that the noise is reduced significantly in almost all directions, however is most dominant for upstream angles, i.e. at 110° and 250°. At last, pressure fluctuations near the surface edges showed that at low frequencies the root generates higher fluctuations than the straight trailing edge, while the tips show less fluctuations. This is in agreement with the observation made for the flow direction near the serration edge.

The research question of this thesis was:
How do trailing edge serrations reduce the noise generated by wings?
On the basis of the observations in this thesis it can be concluded that:
Trailing edge serrations locally accelerate the boundary layer, reduce turbulent fluctuations in the flow and reduce pressure fluctuations on the trailing edge surface which reduces the noise significantly in all directions, but most dominantly upstream. The frequency at maximum noise reduction is defined by a non-dimensional Strouhal number based on the boundary layer displacement thickness at the straight trailing edge of 0.09. Noise reduction is achieved up to a value of 0.23.

5.2 Recommendations for future research

The domain width that was simulated using a direct numerical simulation computation might be insufficient. However, larger spanwise domain size could not be achieved with the computational resources available. For future work it might be advisable to either increase the computational resources or to perform large eddy simulations to increase the domain size. Also the dilatation fields retrieved using the solution give an unexpected result, suggesting an under-resolved direct numerical simulations is not the best method with the computational power available. To make a direct comparison between the direct probes and the acoustic analogies it is advised to position the probes in refinement zones which incorporate the desired viscosity.

Investigate different angles of attack to see the effect for larger pressure gradients at the trailing edge, and to see the effective of non-symmetric flow. Attention should be paid to the aerodynamic forces generated by the addition of trailing edge serrations to expose potential effects in the aerodynamic performance This might be advantageous for application to real life wind turbines as the do operate at non-zero angles of attack.

In combination with the non-zero angle of attack it might be wise to look into flexible serrations. It is suggested that possible reductions are diminished when the local flow is not aligned with the serrations at the trailing edge.

Apart from using the serration in this study one can study the effect of different sizes and shapes of trailing edge add-ons. Future research might also include porous materials in their study as a potential solution for noise mitigation.

Bibliography

C. Aidun and J. Clausen. Lattice-Boltzmann method for complex flows. *Annual Review of Fluid Mechanics*, 42:439–472, 2010.

R. Amiet. Noise due to turbulent flow past a trailing edge. *Journal of Sound and Vibration*, 47(3):387–393, 1976.

C. Arce Léon, F. Avallone, D. Ragni, and S. Pröbsting. PIV investigation of the flow past solid and slitted sawtooth serrated trailing edges. In *54th AIAA Aerospace Sciences Meeting*, volume 1014, 2016a.

C. Arce Léon, R. Merino-Martínez, D. Ragni, F. Avallone, and M. Snellen. Boundary layer characterization and acoustic measurements of flow-aligned trailing edge serrations. Pending review for Experiments in Fluids, 2016b.

F. Avallone, C. Arce Léon, S. Pröbsting, K. Lynch, and D. Ragni. Tomographic-piv investigation of the flow over serrated trailing-edges. In *54th AIAA Aerospace Sciences Meeting (AIAA SciTech)*, 2016.

M. Barone. Survey of techniques for reduction of wind turbine blade trailing edge noise. Technical report, Sandia National Laboratories, SAND2011-5252, 2011.

P. Bhatnagar, E. Gross, and M. Krook. A model for collision processes in gases. i: Small amplitude processes in charged and neutral one-component systems. *Physical Review*, 94 (3):511–525, 1954.

W. Blake. *Mechanics of Flow-induced sound and vibration Volume II: Complex Flow-structure interactions*. Academic Press, 1986.

G. Brès, F. Pérot, and D. Freed. A Ffowcs Williams-Hawkings solver for lattice-Boltzmann based computational aeroacoustics. In *16th AIAA/CEAS Aeroacoustic Conference*. AIAA Paper 2010-3711, 2010.

R. Brionnaud, G. Trapani, M. Chavéz Modena, and D. Holman. Direct noise computation with a lattice-Boltzmann method and application to industrial test cases. In *22th AIAA/CEAS Aeroacoustics Conference*. AIAA Paper 2016-2969, 2016.

T. Brooks, D. Pope, and M. Marcolini. Airfoil self-noise and prediction. Technical report, NASA Reference Publication 1218, 1989.

D. Casalino, A. Ribeiro, E. Feras, and S. Nölting. Lattice-Boltzmann aeroacoustic analysis of the LAGOON landing-gear configuration. *American Institute of Aeronautics and Astronautics Journal*, 52(6):1232–1248, 2013.

H. Chen, S. Chen, and W. Matthaeus. Recovery of the Navier-Stokes equations using a lattice-gas Boltzmann method. *Physical Review A*, 45(8):5339–5342, 1992.

S. Chen and G. Doolen. Lattice Boltzmann method for fluid flows. *Annual Review of Fluid Mechanics*, 30:329–364, 1998.

J. Christophe, S. Moreau, and J. Anthoine. Trailing edge noise computation of a fan blade profile. In *10ème Congrès Français d'Acoustique*, 2010.

N. Curle. The influence of solid boundaries upon aerodynamic sound. *Proceedings of the Royal Society A*, 231(1187):505–514, 1955.

T. Dassen, R. Parchen, J. Bruggeman, and F. Hagg. Results of a wind tunnel study on the reduction of airfoil self-noise by the application of serrated blade trailing edges. Technical report, National Aerospace Laboratory NLR, NLR-TP-96350, 1996. Presented at the 1996 European Union Wind Energy Conference and Exhibition.

A. de Jong. *Aeroacoustic Resonance of Slender Cavities: An experimental and numerical investigation*. PhD thesis, Delft University of Technology, 2012.

W. de Roeck. *Hybrid methodologies for the computational aeroacoustic analysis of confined, subsonic flows*. Phd thesis, Katholieke Universiteit Leuven, 2007.

M. Drela. *XFOIL: An Analysis and Design System for Low Reynolds Number Airfoils*, pages 1–12. Springer Berlin Heidelberg, 1989.

F. Farassat and G. Succi. The prediction of helicopter discrete frequency noise. *Vertica*, 4: 309–320, 1983.

J. Ffowcs Williams and L. Hall. Aerodynamic sound generation by turbulent flow in the vicinity of a scattering half plane. *Journal of Fluid Mechanics*, 40:657–670, 1970.

J. Ffowcs Williams and D. Hawkings. Sound generation by turbulence and surfaces in arbitrary motion. *Philosophical Transactions of the Royal Society A*, 264(1151):321–342, 1969.

T. Geyer, E. Sarradj, and C. Fritzsche. Porous airfoils: Noise reduction and boundary layer effects. In *15th AIAA/CAES Aeroacoustic Conference (30th AIAA Aeroacoustic Conference)*. AIAA Paper 2009-3392, 2009.

T. Geyer, E. Sarradj, and C. Fritzsche. Measurement of the noise generation at the trailing edge of porous airfoils. *Experimental Fluids*, 48:291–308, 2010.

M. Gruber, M. Azarpeyvand, and P. Joseph. Airfoil trailing edge noise reduction by the introduction. In *Proceedings of 20th International Congress on Acoustics*, 2010.

G. Guidati, J. Ostertag, and S. Wagner. Prediction and reduction of wind turbine noise: An overview of research activities in Europe. AIAA Paper 2000-0042, 2000.

K. Habibi, H. Gong, A. Najafi-Yazdi, and L. Mongeau. Numerical simulations of sound radiated from internal mixing nozzles with forced mixers using the lattice Boltzmann method. In *19th AIAA/CEAS Aeroacoustics Conference*. AIAA Paper 2013-2143, 2013.

X. He and L.-S. Luo. Theory of the lattice Boltzmann method: From the Boltzmann equation to the lattice Boltzmann equation. *Physical Review E*, 56(6):6811–6817, 1997.

M. Herr. On the design of silent trailing edges. *New Results in Numerical and Experimental Fluid Mechanics IV, Notes on Numerical Fluid Mechanics 96*, pages 430–437, 2007.

M. Herr and W. Dobrzynski. Experimental investigations in low-noise trailing-edge design. *American Institute of Aeronautics and Astronautics Journal*, 43(6):1167–1175, 2005.

M. Howe. Aerodynamic noise of a serrated trailing edge. *Journal of Fluids and Structures*, 5:33–45, 1991a.

M. Howe. Noise produced by a sawtooth trailing edge. *Journal of Acoustical Society of America*, 90(1):482–487, 1991b.

M. Howe. Trailing edge noise at low Mach numbers. *Journal of Sound and Vibration*, 225(2): 211–238, 1999.

H. Huang, M. Sukop, and X. Lu. *Multiphase Lattice Boltzmann Methods: Theory and Application*. John Wiley & Sons, 2015.

H. Hubbard and K. Shepherd. Aeroacoustics of large wind turbines. *Journal of Acoustical Society of America*, 89(6):2495–2508, 1991.

L. Jones and R. Sandberg. Acoustic and hydrodynamic analysis of the flow around an aerofoil with trailing-edge serrations. *Journal of Fluid Mechanics*, 706:295–322, 2012.

L. Jones and R. Sandberg. Numerical investigation of airfoil self-noise reduction by addition of trailing-edge serrations. In *16th AIAA/CEAS Aeroacoustics Conference*. AIAA Paper 2010-3703, 2010.

H.-J. Kim, S. Lee, and N. Fujisawa. Computation of unsteady flow and aerodynamic noise of naca0018 airfoil using large-eddy simulation. *International Journal of Heat and Fluid Flow*, 27:229–242, 2006.

P.-T. Lew, A. Lyrintzis, B. Crouse, G. Balasubramanian, D. Freed, and L. Mongeau. Noise prediction of a turbulent round jet using the lattice-Boltzmann method. In *13th AIAA/CEAS Aeroacoustics Conference (28th AIAA Aeroacoustics Conference)*. AIAA Paper 2007-3636, 2007.

X. Li, R. Leung, and R. So. One-step aeroacoustics simulation using lattice boltzmann method. *American Institute of Aeronautics and Astronautics Journal*, 44(1):78–89, 2006a.

X. Li, R. So, and R. Leung. Propagation speed, internal energy, and direct aeroacoustics simulation using Lattice Boltzmann Method. *American Institute of Aeronautics and Astronautics Journal*, 44(12):2896–2903, 2006b.

M. Lighthill. On sound generated aerodynamically. I: General theory. *Proceedings of the Royal Society A*, 211(1107):564–587, 1952.

S. Marié, D. Ricot, and P. Sagaut. Comparison between lattice Boltzmann method and Navier-Stokes high order schemes for computational aeroacoustics. *Journal of Computational Physics*, 228:1056–1070, 2009.

F. Mathey. Aerodynamic noise simulation of the flow past an airfoil trailing-edge using a hybrid zonal RANS-LES. *Computer & Fluids*, 37:836–843, 2008.

S. Nölting, G. Brès, P. Dethioux, T. van de Ven, and R. Vieito. A hybrid lattice-Boltzmann/FW-H method to predict sources and propagation of landing gear noise. In *16th AIAA/CEAS Aeroacoustics Conference (28th AIAA Aeroacoustics Conference)*. AIAA Paper 2010-3976, 2010.

A. Oberai, F. Roknaldin, and T. Hughes. Trailing-edge noise due to turbulent flows. Technical report, Boston University, 02-002, 2002.

S. Oerlemans. Wind turbine noise: Primary noise sources. Technical report, National Aerospace Laboratory NLR, NLR-TP-2011-066, 2011.

S. Oerlemans, P. Sijtsma, and B. Lopez. Location and quantification of noise sources on a wind turbine of sawtooth and slitted trailing edge geometries. *Journal of Sound and Vibration*, 299(4-5):869–883, 2007.

S. Oerlemans, M. Fisher, T. Maeder, and K. Kögler. Reduction of wind turbine noise using optimized airfoils and trailing-edge serrations. *American Institute of Aeronautics and Astronautics Journal*, 47(6):1471–1481, 2009.

R. Paterson, P. Vogt, M. Fink, and C. Munch. Vortex noise of isolated airfoils. *Journal of Aircraft*, 10(5):296–302, 1973.

B. Petitjean, R. Drobietz, and K. Kinzie. Wind turbine blade noise mitigation technologies. In *4th International Conference on Wind Turbine Noise*, pages 593–606, 2011.

S. Pope. *Turbulent flows*. Cambridge University Press, 11th edition, 2000.

R. Sandberg and L. Jones. Direct numerical simulations of low Reynolds number flow over airfoils with trailing-edge serrations. *Journal of Sound and Vibration*, 330:3818–3831, 2011.

M. Sanjosé and S. Moreau. Direct self-noise simulation of the installed controlled diffusion airfoil. In *17th AIAA/CEAS Aeroacoustic Conference (32nd AIAA Aeroacoustic Conference)*. AIAA Paper 2011-2716, 2011.

M. Sanjosé, C. Méon, V. Masson, and S. Moreau. Direct numerical simulation of acoustic reduction using serrated trailing-edge on an isolated airfoil. In *20th AIAA/CEAS Aeroacoustic Conference*. AIAA Paper 2014-2324, 2014.

A. Schneider, D. Conrad, and M. Böhle. Lattice Boltzmann simulation of the flow field in pump intakesa new approach. *Journal of Fluids Engineering*, 137(3):1–10, 2015.

C. Sesor, P. Sagaut, and A. Belanger. A numerical aeroacoustics analysis of a detailed landing gear. In *10th AIAA/CEAS Aeroacoustics Conference*. AIAA Paper 2004-2884, 2004.

S. Succi. *The Lattice Boltzmann Equation for Fluid Dynamics and Beyond*. Oxford University Press Inc., 2001.

C. Tam. Discrete tones of isolated airfoils. *Journal of the Acoustical Society of America*, 55 (6):1173–1177, 1974.

C. Tam. Computational aeroacoustics: An overview of computational challenges and applications. *International Journal of Computational Fluid Dynamics*, 18(6):547–567, 2004.

W. van der Velden, A. van Zuijlen, and D. Ragni. Flow topology and noise emission around straight, serrated and slitted trailing edges using the lattice Boltzmann methodology. In *22nd AIAA/CEAS Aeroacoustics Conference*. AIAA 2016-3021, 2016.

M. Wang and P. Moin. Computation of trailing-edge flow and noise using large-eddy simulation. *American Institute of Aeronautics and Astronautics Journal*, 38(12):2201–2209, 2000.

J. Winkler, S. Moreau, and T. Carolus. Large-eddy simulation and trailing-edge noise prediction of an airfoil with boundary-layer tripping. In *15th AIAA/CEAS Aeroacoustic Conference (30th AIAA Aeroacoustic Conference)*. AIAA Paper 2009-3197, 2011.

T. Zhu, M. Sturm, and T. Carolus. Experimental and numerical investigation of tip clearance noise of an axial fan using a lattice Boltzmann method. In *21st International Congress on Sound and Vibration*, 2014.